# Structural insights into p300 regulation and acetylation-dependent genome organisation

Ziad Ibrahim[1], Tao Wang[2], Olivier Destaing[2], Nicola Salvi[3], Naghmeh Hoghoughi[2], Clovis Chabert[2], Alexandra Rusu[1], Jinjun Gao[4], Leonardo Feletto[1], Nicolas Reynoird[2], Thomas Schalch[1], Yingming Zhao[4], Martin Blackledge[3], Saadi Khochbin[2] & Daniel Panne[1,*]

[1]Leicester Institute of Structural and Chemical Biology, Department of Molecular and Cell Biology, University of Leicester, Leicester, UK

[2]CNRS UMR 5309, INSERM U1209, Université Grenoble Alpes, Institute for Advanced Biosciences, Grenoble, France.

[3]Institut de Biologie Structurale, CNRS, CEA, UGA, Grenoble, France

[4]Ben May Department of Cancer Research, The University of Chicago, Chicago, IL 60637, USA.

*Correspondence: daniel.panne@leicester.ac.uk

## Summary

**Histone modifications are deposited by chromatin modifying enzymes and read out by proteins that recognize the modified state. BRD4-NUT is an oncogenic fusion protein of the acetyl lysine reader BRD4 that binds to the acetylase p300 and enables formation of long-range intra- and interchromosomal interactions. We here examine how acetylation reading and writing enable formation of such interactions. We show that NUT contains an acidic transcriptional activation domain that binds to the TAZ2 domain of p300. We use NMR to investigate the structure of the complex and found that the TAZ2 domain has an autoinhibitory role for p300. NUT-TAZ2 interaction or mutations found in cancer that interfere with autoinhibition by TAZ2 allosterically activate p300. p300 activation results in a self-organizing, acetylation-dependent feed-forward reaction that enables long-range interactions by bromodomain multivalent acetyl-lysine binding. We discuss the implications for chromatin organisation, gene regulation and dysregulation in disease.**

**Keywords:** Chromatin modification, Acetylation, bromodomain, BRD4, acetyltransferase, p300, transcription factor, activation domain, gene regulation, NMR

## Introduction

Chromosome capture experiments have led to the identification of two major mechanisms that are behind large-scale chromosome organisation[1,2]: (1) at shorter genomic distances, genomes are organized into topologically associating domains[3,4] which arise through the process of loop extrusion by cohesin; (2) at longer-range genomic distances, genomes are spatially compartmentalised into active, euchromatic and inactive, heterochromatic regions[5,6].

One of the main mechanisms driving genome compartmentalisation is thought to be selective self-association of active or inactive regions and physical constraints including association with architectural elements[7,8]. One hypothesis is that 'readers' of histone modifications seed 'condensation' reactions as a function of the histone modification state[6,9]. It has been proposed that compartmentalisation arises specifically due to attractions between heterochromatic regions, possibly driven by polymer-polymer interactions and liquid-liquid phase separation (LLPS)[10,11]. Whether heterochromatic compartments form through LLPS or other mechanisms is controversial[12-15].

Histone acetylation counteracts heterochromatinization and has long been associated with chromatin decondensation and euchromatic chromatin regions[16]. Targeting of heterochromatin with acidic transcription factor (TF) activation domains (ADs) or treatment with deacetylase inhibitors results in hyperacetylation, decondensation and relocation to the nuclear interior even in the absence of active transcription[17-23].

Numerous TFs associate through their ADs with a small set of co-activators including Mediator and the acetylases CBP and its paralogue p300 (also known as KAT3A and KAT3B respectively; hereafter 'p300' for short)[24-29]. p300 has long been known to be important in integrating multiple signal transduction pathways in the nucleus and enabling enhancer-mediated transcription[30-32]. Intriguingly, it has been proposed that spatial sequestration of heterochromatin at the nuclear lamina requires TF-mediated retention of p300 in euchromatin[33]. Quantitative Mass Spectrometry experiments show that p300 is present at limiting concentrations in the nucleus while HDAC co-repressors are in large excess[34]. As p300 is responsible for up to a third of nuclear acetylation[35], TF-mediated competition for and retention of these essential and limiting co-activators in euchromatic regions could be a key driver event that not only shapes gene specific transcription but also eu- and heterochromatic genome compartmentalisation.

It has been proposed that transcriptional control may be driven by the formation of phase-separated condensates[36]. Accordingly, condensates of TF ADs[37], co-activators and the transcriptional machinery have all been proposed to be relevant for transcriptional regulation[38-43]. p300 contains an ordered catalytic 'core' domain including a HAT- and bromodomain (BD) and several domains that form promiscuous interactions with the disordered ADs of hundreds of cellular TFs (Fig. 1a)[44,45]. These interactions domains are separated by long, intrinsically disordered regions (IDRs). p300 is activated by autoacetylation[46], a reaction that can be controlled by cellular signalling through TF activation and dimerisation[47]. The p300 core contains a RING and TAZ2 domain that have an autoinhibitory function[44,47]. Perturbation of the autoinhibitory function of the RING and TAZ2 domains by mutation leads to constitutive p300

activation and formation of nuclear droplets that co-localise with p53. These droplets are dispersed upon HAT or BD inhibition, suggesting that a form of phase separation (we here use the more general term 'condensation') occurs through an acetylation-dependent 'read-write' mechanism[47]. Other data indicate that p300 forms nuclear condensates through the 'core' domain[48]. Co-condensation of p300 with TFs on enhancer loci is thought to enable activation of p300's catalytic activity thus allowing the recruitment of acetylation-dependent coactivators, including the BD - and extraterminal domain-containing (BET) protein BRD4[49].

BET proteins have long been associated with the control of large-scale nuclear structure and chromatin organization. BRDT, a testes-specific BET, mediates histone acetylation-dependent chromatin condensation[50] and is required for stage-specific gene expression and acetylation-dependent histone removal during spermatogenesis[51-53]. Similarly, BRD4 has been linked both to gene-specific[54] and higher-order chromatin organisation[55,56]. In yeast, the BET protein BDF1 maintains physical genome barriers by preventing spreading of heterochromatin[57]. *In vitro* data show that under specific buffer conditions, chromatin can undergo LLPS which can be modulated by acetylation and BRD4 binding[58]

BRD4 also forms condensates in cells[39]. *In vitro* and *in vivo* experiments with systems inducing high local concentration suggest that a C-terminal IDR drives the condensation reaction[39,59]. However, a BRD4 isoform lacking the C-terminal IDR also forms condensates in cells[60]. Other data indicate that BRD4 clustering does not depend on IDR-mediated condensation but on DNA and BD-acetyl-lysine recognition which possibly enables long-range enhancer-promoter communication[61]. At a larger scale, such acetylation-dependent long-range interactions could enable selective self-association of euchromatic regions and provide a link between genome topology and gene regulation. It is therefore important to understand the underlying 'read-write' mechanisms that drive such long-range interactions.

BRD4-NUT is an oncogenic fusion protein that drives NUT carcinoma, one of the most aggressive human solid malignancies known[62]. NUT is normally expressed in post-meiotic spermatogenic cells, where it interacts with p300 and triggers genome-wide histone hyperacetylation, which enables recruitment of BRDT, histone-to-protamine exchange and chromatin compaction during spermatogenesis[53]. In the oncogenic fusion protein, NUT binds to and activates p300 which drives an acetylation- and BRD4 BD-dependent 'feed-forward' loop that leads to formation of hyperacetylated nuclear 'foci' visible by light microscopy[62-64], that resemble foci seen in cells expressing constitutively activated p300[47]. These foci correspond to large chromosomal 'megadomains' (100 kb to 2 Mb) that are enriched for BRD4-NUT, p300 and acetylated histones[65-67]. Megadomains form in the absence of transcription and engage in very long-range acetylation-dependent inter- and intrachromosomal interactions[68].

The BRD4-NUT model thus exemplifies how a modification of BRD4 enables recruitment and activation of p300 and establishment of a self-organizing feed-forward reaction that results in chromatin hyperacetylation and long-range contact. The underlying mechanisms could have broad implications for our understanding of how 'reading' and 'writing' of chromatin acetylation control gene expression and how dysregulation of this process leads to aggressive forms of disease.

Here we use the BDR4-NUT/p300 system to dissect the mechanism that drives large-scale chromatin organization. We determined the element of BRD4-NUT required for interaction with p300. We found that the NUT portion of the fusion protein contains an acidic AD that interacts with the p300 TAZ2 domain, a common binding site for numerous TF ADs. We investigate the solution behavior of the complex and found that interaction with the TAZ2 domain stimulates p300 HAT activity. Our data indicate that the TAZ2 domain has an auto-inhibitory function that is relieved upon TAZ2 ligand-binding. We systematically probed which elements of BRD4-NUT and p300 drive large scale chromatin condensation in cells. We found that condensation depends on a feed-forward mechanism that involves allosteric activation of p300 by binding of NUT to the p300 TAZ2 domain, nucleation of the condensation reaction through BRD4 and p300 BD-acetyl-lysine binding and that BD multivalency is required. We found that Adenoviral E1A, another TAZ2 ligand, or mutations associated with cancer that interfere with TAZ2 autoinhibition also activate p300. Our data reveal how activation of p300 establishes a self-organising positive feedback mechanism and how an acetylation-dependent read-write mechanism drives larger-scale chromatin architecture.

## Results

### Identification of an acidic activation domain in NUT

Previous data showed that a region spanning BRD4-NUT amino acids 347-588 (NUT F1c; NUT numbering is used; 1060-1307 in BRD4-NUT) directly interacts with p300 (Fig. 1a,b)[63]. To map the interaction further, we produced a series of deletions within NUT and assayed their interaction with p300 using co-sedimentation and GST pulldown assays. NUT fragments that contained amino acids 396-482 generally co-sedimented with the p300 core-CH3, the isolated p300 CH3 or TAZ2 domains (Fig. S1a,b; Fig. S2a-f).

The TAZ2 domain forms dynamic interactions with short ~30 amino acid transcription factor activation domains (ADs) that are unrelated in sequence but generally share net negative charge, hydrophobic, and aromatic residues that are typically intrinsically disordered (IDR) in isolation[45]. Accordingly, sequence analysis revealed that the region of NUT is predicted to be disordered, and negatively charged with modest propensity to self-aggregate (Fig. 1c). A luciferase assay confirmed that the isolated NUT region can stimulate transcription (Fig. S1c), in agreement with previous data showing that tethering of NUT on chromatin is sufficient to induce transcriptional activation[67]. We therefore conclude that NUT contains an acidic AD that directly interacts with the TAZ2 domain of p300 (Fig. 1b).

The high percentage of negatively charged amino acid residues in ADs is thought to prevent hydrophobic collapse while the distribution of charges maintains the conformational ensemble in a more expanded state leaving the charged and hydrophobic side chains exposed to the solvent and binding partners[69]. Accordingly, analysis by size-exclusion chromatography–multi-angle laser-light scattering (SEC–MALS) showed that a NUT fragment spanning amino acids 347-480 (NUT4) is monomeric and monodisperse in solution with a large hydrodynamic radius, consistent with an extended conformation (Fig. 1d). The TAZ2:NUT4 complex formed a 1:1 complex with a reduced hydrodynamic radius, indicative of conformational compaction upon binding (Fig. 1d).

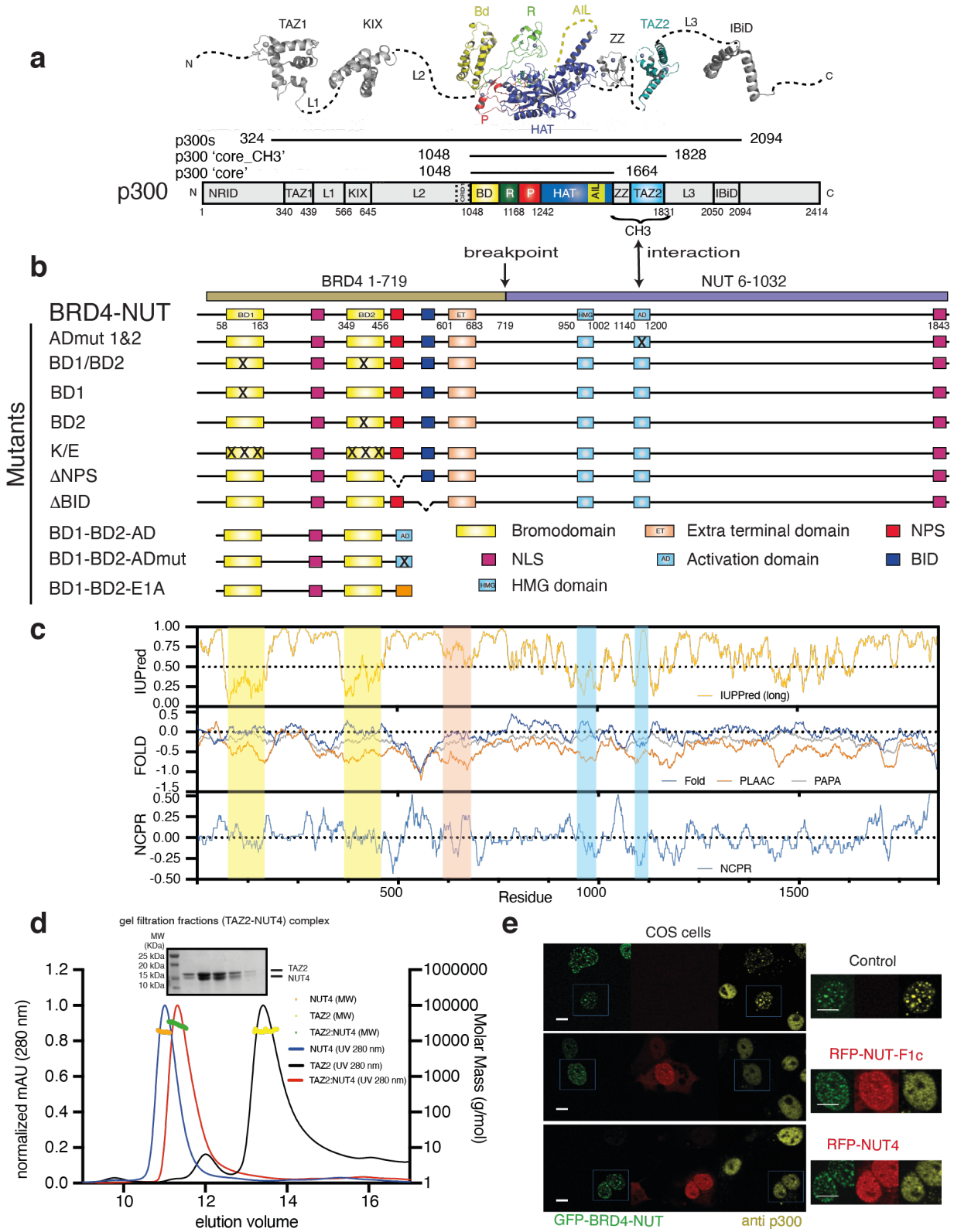


**Figure 1. Identification of an acidic activation domain in NUT**. **a**, Domain structure of p300 and **b**, BRD4-NUT constructs. **c,** IUPred, prediction of intrinsic disorder; FOLD, folding prediction using the foldindex (blue), PLAAC (**P**rion-**L**ike **A**mino **A**cid **C**omposition; orange) and PAPA (**P**rion **A**ggregation **P**rediction **A**lgorithm; gray) analysis, NCPR (**N**et **C**harge **P**er **R**esidue with a sliding window of 10 residues of the BRD4-NUT protein. **d**, SEC-MALLS analysis of the TAZ2 domain of p300 alone (black), NUT4 alone (blue) and the complex between TAZ2 and NUT4 (red). SDS-PAGE analysis of the peak fractions of the TAZ2-NUT4 complex is shown. **e,** Competition analysis: Cos7 cells were transfected with constructs expressing GFP-BRD4-NUT (green) alone or co-transfected with RFP-NUT-F1c and RFP-NUT4 (red). Immunofluorescence with anti-p300 antibody was used to visualize endogenous p300. Scale bars, 10 µm.

178 Co-expression of NUT F1c can prevent condensate formation in the nucleus by acting as a
179 dominant negative inhibitor for the p300-NUT interaction[63,67]. Accordingly, overexpression of
180 RFP-NUT F1c, -NUT4, or -NUT2 but not -NUT1 or -NUT3 reduced p300 foci in COS cells
181 (Fig. 1e, Fig. S2g). As AD function is usually confined to short sequences, we further mapped
182 the interaction by limited proteolysis followed by in-gel acid hydrolysis and mass spectrometry
183 (Fig. S1d). Fragments spanning amino acids 396-482 (NUT9) or a peptide spanning 458-482
184 (NUT10) all bound to the TAZ2 domain (Table S1).
185
186 **TAZ2-NUT interaction.**
187 NMR spectra of NUT7, spanning 448-492, feature little dispersion of $^{1}$H resonances (Fig. 2a),
188 indicating that the protein is largely disordered in solution. We used a series of 3D experiments
189 (see Methods) to assign backbone resonances of NUT7. Secondary structure propensities (SSP)
190 calculated using $^{13}$Cα, $^{13}$C' and $^{15}$N chemical shifts show that amino acids 451-472 have a
191 significant tendency to sample helical conformations in solution (Fig. 2b). We conclude that the
192 NUT7 AD is an IDR in isolation with a pre-organised N-terminal α helix.
193
194 We monitored binding to the TAZ2 domain by collecting a series of $^{1}$H, $^{15}$N-HSQC spectra of
195 $^{15}$N-labeled NUT7 mixed with increasing concentrations of TAZ2 (Fig. 2a). Chemical shift
196 perturbations (CSP) showed that several NUT7 backbone amide resonances, including A450,
197 L451, G460-A464, V467 and E475 were perturbed upon addition of an equimolar amount of
198 TAZ2 while resonances from the C-terminus of NUT7 do not appear to shift significantly upon
199 addition of TAZ2 (Fig. 2c). Thus, the N-terminal α-helical segment of NUT7 is involved in
200 TAZ2 binding. Addition of equimolar amounts of unlabelled NUT7 to $^{15}$N-labeled TAZ2
201 showed significant CSPs of resonances corresponding to residues R1737, I1739, M1761, R1763,
202 V1765, Q1766, T1768, K1783, Q1784, I1809 (Fig. 2a, c), that are mostly located on the surface
203 of TAZ2.
204
205 To understand the binding mode, we measured both $^{13}$C- and $^{15}$N-HSQC-NOESY spectra on a
206 sample of $^{15}$N,$^{13}$C-labelled TAZ2 to which one equivalent of unlabelled NUT7 was added. We
207 also measured $^{15}$N-HSQC-NOESY spectra on $^{15}$N-labelled NUT7 in admixture with one
208 equivalent of unlabelled TAZ2. The NOESY spectra contain very few cross-peaks that can be
209 unambiguously assigned to intermolecular contacts most likely due to extensive dynamic
210 fluctuations of NUT7 even in the bound state. One contact is made between the backbone amide
211 hydrogen of S1726 in TAZ2 and the backbone amide hydrogen of residue L463 and the Hβ of
212 A464 in NUT7. Because of relative sparsity and ambiguity of structural restraints, we used
213 HADDOCK[70] to derive a structural model of the interaction consistent with the observed
214 spectroscopic changes (Fig. 2d and e). NMR restraints and structural statistics are summarized in
215 Table S2. On the basis of this model, it appears that the N-terminus of NUT7 folds into an
216 amphipathic helix that binds a hydrophobic groove in the interface between helices α1/α2/α3 on
217 the surface of TAZ2 (Fig. 2d). Only the NUT backbone residues P448 to A464 are well ordered
218 while residues at the C-terminus (Q465-D492) do not interact with TAZ2 and remain disordered.
219 A set of hydrophobic side chains of NUT L449, A450, L451, L455, L461 are in contact with
220 TAZ2 residues I1735, M1761, V1764, I1781 (Fig. 2d). The interaction is further stabilised by
221 electrostatic interactions involving NUT residues E453, E454, E456, E458, E459 and TAZ2
222 residues R1737, S1754, S1757 and K1760 (Fig. 2d). In summary, similar to other TAZ2:AD

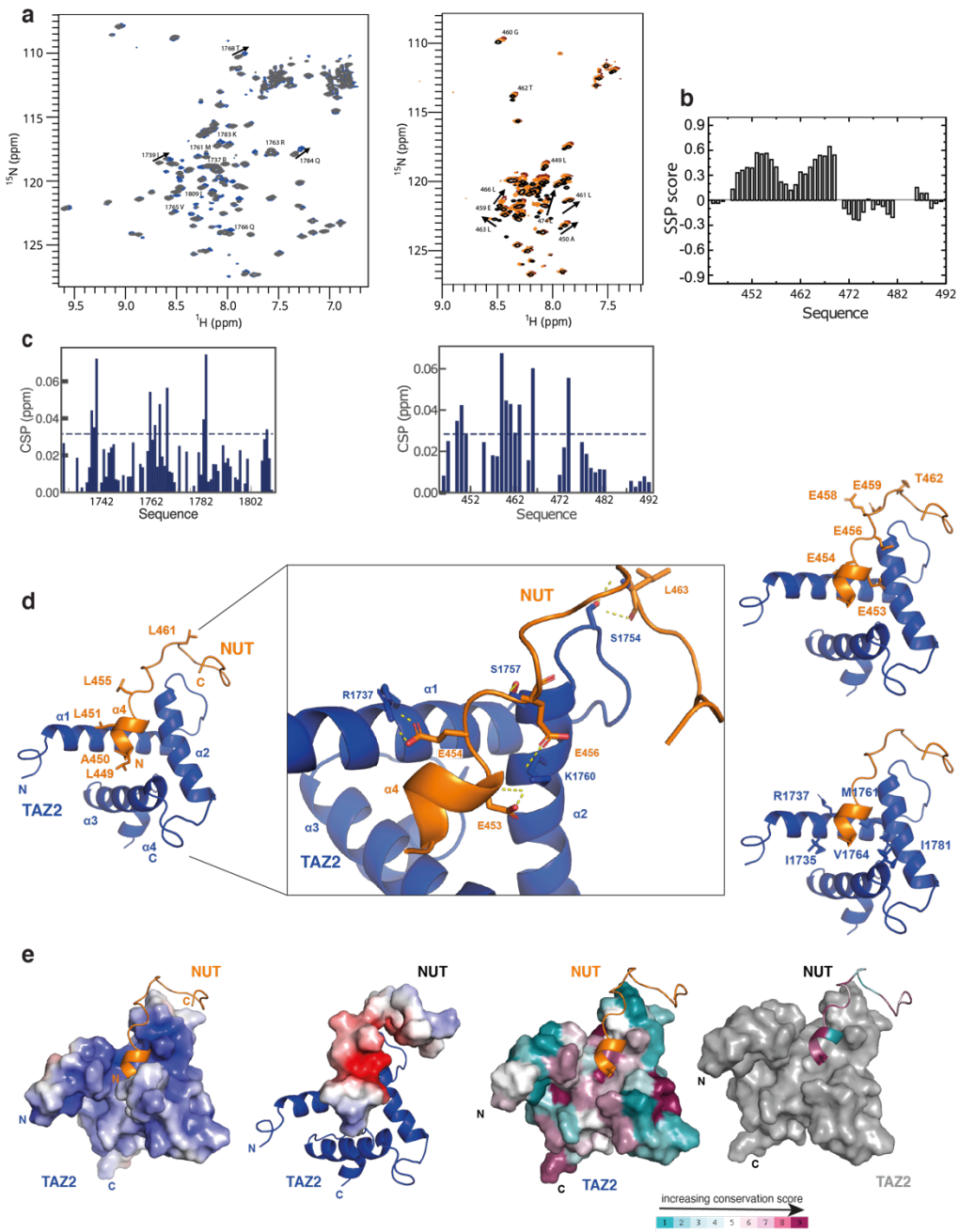


**Figure 2. TAZ2:NUT interaction**. **a**, (Left) Overlay of $^{1}$H-$^{15}$N HSQC spectra of free TAZ2 (black) and after addition of one molar equivalent of NUT7 (448-492) (blue). Arrows indicate chemical shift changes for individual cross-peaks. (Right) Overlay of $^{1}$H-$^{15}$N HSQC spectra of free NUT7 (448-492) and after adding half (orange) and one (brown) molar equivalent of TAZ2. Arrows indicate chemical shift changes for individual cross-peaks. **b**, Secondary structure propensities (SSP) plot of the NUT (448-492) fragment in its free state. positive values on the Y-axis indicate a-helical propensity, the X-axis is the amino acid sequence. **c**, (Left) Chemical shift perturbations on TAZ2 upon adding one molar equivalent of unlabeled NUT7 (448-492). (Right) Chemical shift perturbations on NUT7 (448-492) upon adding one molar equivalent of unlabeled TAZ2. **d**, (Left) Ribbon representation of lowest energy NMR model of the TAZ2 (blue)-NUT (orange) complex. Hydrophobic residues on the surface of NUT are shown. (middle) Zoom-in view of the interface between NUT (orange) and TAZ2 (blue). Residues on both sides implicated in the interaction as well as the hydrogen bonding network are shown. (Right) acidic residues on the surface of NUT (top) as well as hydrophobic and basic residues on the surface of TAZ2 (bottom) are shown. **e,** TAZ2 and NUT7 (448-492) are surface rendered and colored according to electrostatic potential (left) and sequence conservation (right).

223 interactions, a positively charged TAZ2 domain interacts with a negatively charged NUT AD
224 (Fig. 2e). The key interfacial binding surfaces are conserved in p300 and NUT (Fig. 2e).
225
226 **Analysis of the TAZ2:NUT interaction**
227 As ADs are frequently bi-partite and the NUT7 fragment in our structure only partially engages
228 the TAZ2 binding surface, we further explored the region N-terminal of NUT7. We found using
229 HSQC competition, that the NUT7 fragment is unable to displace p53 from the surface of TAZ2
230 when added to the complex (Fig. S3d). Biolayer Interferometry (BLI) experiments showed that
231 NUT8 (396-470) bound to TAZ2 with a dissociation constant of $K_d$ = 0.96 +/- 0.29 μM (Fig. 3a,
232 b). Alanine substitutions of conserved residues in the region spanning 447-462 (mut3, Fig. 3c),
233 the main binding epitope in NUT7, did not abolish TAZ2 binding in GST-pulldowns, but
234 reduced TAZ2 binding affinity (Fig. 3b, Fig. S3a,b). Additional Alanine substitution of L436,
235 L440, L441 (mut4, Fig. 3c) further reduced TAZ2 affinity (Fig. 3b). In contrast, binding was
236 largely abolished by additional mutation to Alanine of L410, L411, Y413, L427, C428, F423,
237 V424, V427, V430 and I431 (mut1, Fig. 3b-d, Fig. S3a). As alanine repeat expansion can alter
238 transcription factor condensation properties[71], we also generated a NUT variant containing
239 mostly Glycine, Serine and charge reversal mutations (mut2, Fig. 3c). Mut2 also failed to bind
240 TAZ2 in BLI and GST-pulldown experiments (Fig. 3b-d, Fig. S3a).
241
242 As mutation of isolated binding epitopes reduced but did not abolish TAZ2 binding, we conclude
243 that the NUT AD is made up of subdomains that contain short amphipathic interaction motifs
244 that synergise to enable high affinity binding. TF ADs frequently bind p300 through a minimal
245 ΦXXΦΦ motif (X is any residue and Φ is hydrophobic), frequently LXXLL[72]. The NUT AD
246 contains several such conserved motifs most of which are predicted to engage TAZ2 (Fig. 3c,e).
247
248 In our structure, the isolated AD sub-domain in NUT7 is positioned at the interface of the TAZ2
249 α1, α2 and α3 helices, which frequently functions as a docking site for TF ADs that typically
250 adopt helical structure upon binding (Fig. S3f). AlphaFold (AF) computational models predict 5
251 helices for NUT (Fig. 3e) that engage the protein interaction surfaces of TAZ2 (Fig. 3f, Fig.
252 S3c,g)[73,74]. In the model, the NUT7 AD is re-positioned while the TAZ2 α1, α2, α3 surface is
253 occupied by α3 of the NUT AD. Structure determination of the TAZ2 domain in complex with
254 the entire NUT AD was not possible as NMR spectra suffered from severe broadening (data not
255 shown). As (1) isolated AD sub-domains can interact with alternate TAZ2 surfaces[75] and (2) as
256 the residues that impair binding are located in the predicted TAZ2-NUT binding interface, these
257 data provide a reasonable model for NUT-p300 interaction.
258
259 **The role of the TAZ2 domain in p300 regulation and substrate acetylation**
260 Previous data show that NUT stimulates p300 auto- and histone acetylation in cells and *in*
261 *vitro*[53,63]. The AF model of p300 suggests that the TAZ2 domain is positioned over the p300
262 HAT active site (Fig. 4a). The TAZ2 C-terminal helix (amino acids 1806-1836) is sandwiched
263 between the RING and HAT domains proximal to the lysine substrate-binding tunnel in a
264 conformation that is incompatible with substrate access. In contrast, a model in the presence of
265 NUT AD shows that the TAZ2 domain is displaced from the HAT active site (Fig. 4b). One
266 possibility is that the TAZ2 domain auto-inhibits the HAT domain and that this auto-inhibition is
267 relieved upon ligand-binding to the TAZ2 domain. As the TAZ2 domain binds numerous

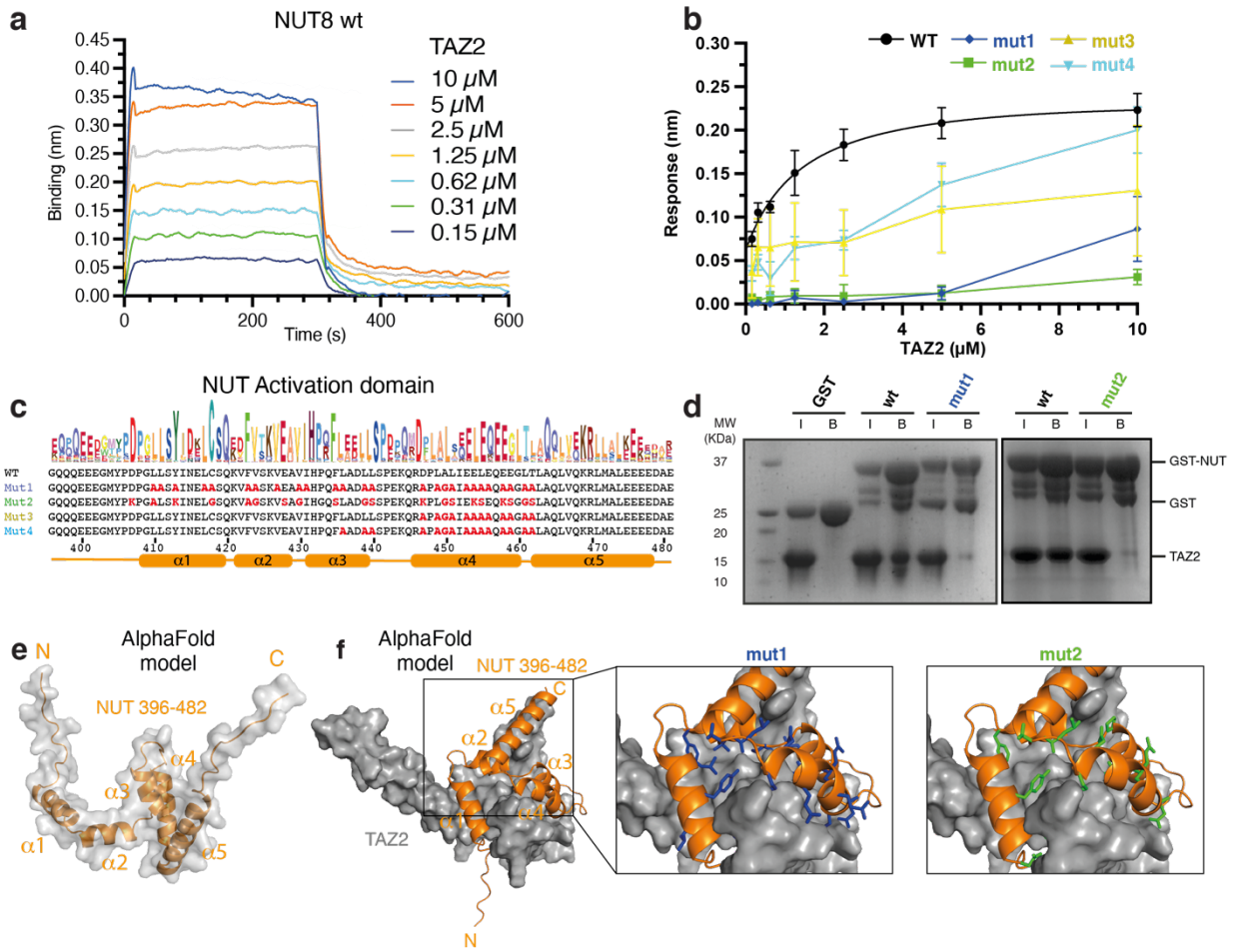


**Figure 3. Analysis of the TAZ2-NUT interaction. a**, Representative Biolayer Interferometry (BLI) profiles of p300 TAZ2-NUT binding from which the steady-state data were derived. **b**, Steady state analysis of p300 TAZ2 interaction with wild-type and NUT mutants using BLI. Error bars represent the standard deviations from three technical replicate experiments. **c**, Sequences of the NUT AD and mutants (in bold red) used. Top: Skylign plot showing NUT AD sequence conservation; Bottom: predicted secondary structure. **d**, GST pulldown analysis of TAZ2 and NUT8 (396-470) wild type and mutants 1 and 2. **e,** AlphaFold prediction of NUT (396-482) structure. **f**, Left: AlphaFold prediction of the TAZ2-NUT complex structure. Right: mutated residues in NUT mutant 1 (blue) and 2 (green) are shown.

268 transcription factor ADs, such a TAZ2-mediated control mechanism may be broadly relevant and
269 a key aspect of how TFs control chromatin acetylation and gene regulation.
270
271 To test this model, we incubated increasing amounts of GST-NUT8wt with p300s (amino acids
272 324-2094) in the presence of [$^{14}$C] acetyl coenzyme A. Addition of NUT WT but not mut1
273 stimulated p300 autoacetylation in a dose-dependent manner (Fig. 4c). Despite the identical
274 number of lysine amino acids, only NUT WT but not mut1 was acetylated by p300. Other NUT
275 fragments that contain the AD also activated p300 (Fig. S4a,b). These data suggest that the
276 TAZ2 domain autoinhibits p300 and that AD-TAZ2 interaction relieves autoinhibition.
277 Accordingly, acetylation reactions with the core domain of p300, lacking TAZ2 (Fig. 1a; p300
278 amino acids 1048-1664), showed that p300 autoacetylation is not stimulated by the presence of
279 NUT WT and both WT and mutant substrates are acetylated at equal rates (Fig. 4d). Another
280 classic TAZ2 ligand, Adenoviral E1A also showed a dose-depended stimulation of p300s auto-
281 and substrate acetylation (Fig. 4e).
282
283 Recent data indicate that p300 directly engages nucleosome core particles (NCPs) through its
284 ZZ[76] and TAZ2 domains[77]. Would then NCP engagement also activate p300? In accordance with
285 this possibility, it has been shown that the TAZ2 domain is required for efficient acetylation of
286 H3K27, while curbing activity towards other lysine residues within nucleosomes[77]. To test this
287 model, we generated homogeneous 'structure-grade' NCPs as shown by single particle cryoEM
288 (Fig. S4f, Table S3). p300 variants containing the TAZ2 domain, as well as the isolated TAZ2
289 domain directly bound to NCPs in EMSA experiments (Fig. S4c,d,e). Addition of increasing
290 amounts of NCPs stimulated auto-acetylation of p300s but not p300 core (Fig. 4f).
291
292 Cross-linking mass spectrometry experiments showed that surface residues from the p300
293 Bromo-, RING, PHD and TAZ2 domains directly engage the N-terminal regions of Histone H3
294 and H2A (Fig. S4i,j). Label free quantitative mass spectrometry experiments showed that p300
295 core acetylated most lysine residues indiscriminately in Histones H2B, H3 and H4 while p300s
296 showed a more selective acetylation pattern (Fig. S4g,h). We therefore conclude that direct NCP
297 binding through the TAZ2 domain can stimulate p300 activation but contributes modestly to
298 substrate specificity.
299
300 To further test the autoinhibition model, we truncated amino acid residues Δ1813-1838 of the
301 TAZ2 domain (Fig. 4a). Deletion of the C-terminal helix resulted in the formation of p300
302 nuclear condensates (Fig. 4g) that are typically seen upon p300 activation[47]. p300 mutations
303 found in cancer cell lines that truncate the TAZ2 domain (Fig. S4k) also result in p300
304 activation[78,79]. Together, we conclude that the TAZ2 domain autoinhibits p300 HAT activity.
305 Interaction of TF ADs with the TAZ2 domain allosterically regulates p300 HAT activation by
306 relief of autoinhibition. Mutations that interfere with TAZ2 autoinhibition are found in cancer.
307
308 **Mechanism of condensation of BRD4-NUT and p300**
309 BRD4-NUT forms hyperacetylated chromatin megadomains in patient tumors[63,65,68]. Formation
310 of such megadomains can be reproduced by expression of BRD4-NUT in heterologous cell
311 lines[63,65,68]. As there is strong evidence that this system reproduces the phenoptype seen in
312 patient cells, we consider it as physiologically relevant, at least with respect to the biophysical
313 properties of the condensation reaction. We generated a series of GFP-BRD4-NUT variants and

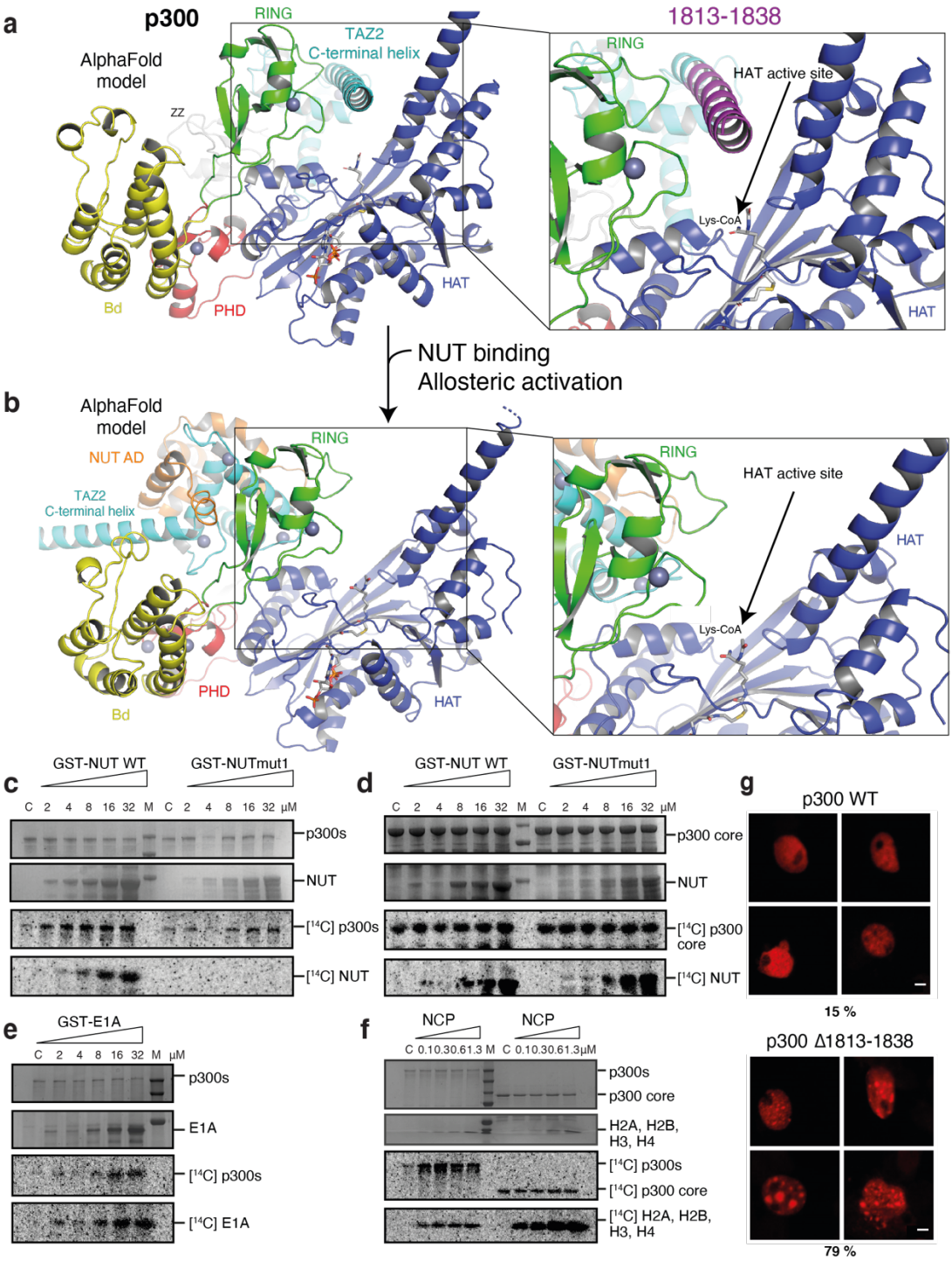


**Figure 4. Role of the TAZ2 domain in p300 regulation and substrate acetylation. a**, AlphaFold prediction of p300 core-CH3 (1048-1838) structure. The structure is coloured according to domain structure. The TAZ2 domain is positioned in the HAT active site thus autoinhibiting substrate access. The TAZ2 C-terminal helix deletion (Δ1813-1838) is coloured in magenta **b,** NUT AD binding displaces the TAZ2 domain from the HAT active site thus enabling allosteric HAT activation. **c,** p300s or **d**, p300 core were incubated with [$^{14}$C]Acetyl-CoA in the presence or absence (C: p300 alone) of increasing concentrations of wild type or mut1 NUT8 (396-470), **e**, Increasing concentrations of GST-E1a we incubated with p300s, **f**, Increasing concentrations of NCPs were incubated with p300s or p300 core. Panels c-f: Top two images: Analysis by SDS–PAGE followed by Coomassie staining. Bottom two images: $^{14}$C phosphor imaging. Representative data of three independent experiments are shown. **g**, Cos7 cells were transfected with the HA-tagged p300 WT (top) or p300 Δ1813-1838 (bottom) and analysed by anti HA immunofluorescence. Four representative nuclei are shown. The percentage of cells showing condensates (n=100 cells) is indicated. Scale bars, 5 μm.

314 assessed their propensity to interact with p300 and form co-condensates in the cell nucleus. Co-
315 immunoprecipitation experiments showed that wild-type GFP-BRD4-NUT but not the AD
316 mutants bound to endogenous p300 (Fig. 5a). In agreement with our *in vitro* data, the wild-type
317 but not mutant variants showed a signal at the level of GFP-BRD4-NUT when probed with an
318 anti-acetyl lysine antibody (Fig. 5a). GST-pulldowns in nuclear extracts using a purified GST-
319 NUT8wt fragment showed signal for p300 only for the wild-type but not the AD mutant variants
320 (Fig. 5b). Thus, mutation of the NUT AD interferes with p300 interaction and BRD4-NUT
321 acetylation in cells, as also seen with the corresponding fragments *in vitro* (Fig. 4c).
322
323 Co-transfection experiments showed that GFP-BRD4-NUTwt and RFP-p300 formed nuclear co-
324 condensates (Fig. 5c; row 1; for quantification see Tables S4 and S5) both in co-transfected and
325 RFP-p300 negative cells. Thus, condensation of GFP-BRD4-NUTwt not only concentrates but
326 also depletes p300 from other areas of the nucleus. These condensates were independent of the
327 NUT AD as mutant variants still formed condensates that co-localized with p300 (Fig. 5c; row
328 2&3) and acetylated chromatin (Fig. S5a). Mutation of the acetyl-lysine binding pocket in BD1
329 (N140A) and BD2 (N433A) completely abolished GFP-BRD4-NUT and RFP-p300 co-
330 condensation (Fig. 5c; row 4). To assess the model that BRD4 multivalency drives the
331 condensation reaction[58], we mutated BD1 and BD2 individually. We found that mutation of BD1
332 but not BD2 largely abolished condensation (Fig. 5c; row 5, 6). Thus, the acetyl-lysine binding
333 ability of BD1 is required to nucleate BRD4-NUT and p300 co-condensation.
334
335 We reported previously that BRDT interacts with nucleosomes through its first (BD1), but not
336 second (BD2) bromodomain, and that acetylated Histone recognition by BD1 is complemented
337 by a direct BD1–DNA interaction[80]. Another report indicates that DNA binding promotes
338 condensation of a short BRD4S 'isoform' *in vitro*[60]. We therefore introduced charge inversion
339 mutations in a conserved, basic surface patch in BD1 (R68E, K72E, K76E) that is involved in
340 DNA binding in BRDT[80] and in the equivalent BD2 amino acids (S358E, K362E, A366E).
341 Mutation of the basic patch abolished condensation (Fig. 5c; row 7). Thus, we propose that
342 BRD4 BD-DNA interaction facilitates acetylation-dependent NCP binding and chromatin
343 condensation in cells.
344
345 We also probed the BRD4 N-terminal cluster of phosphorylation sites (NPS) and the basic
346 residue-enriched interaction domain (BID), elements that have been proposed to enable BRD4
347 regulation by phosphorylation[81]. Deletion of the NPS did not interfere with condensation while
348 removal of the BID reduced condensation (Fig. 5c; row 8, 9). A minimal BD1-BD2 variant fused
349 to the AD but not an AD Mut1 variant (Fig. 1b) still formed p300 co-condensates (Fig. 5c; row
350 10, 11, Movie S1). The BD1-BD2-AD fusion protein but not the AD Mut1 variant was still able
351 to co-IP p300 from cells indicating that the ability to interact with p300 is maintained in the
352 fusion protein (Fig. S5c). Fusion of the minimal BD1-BD2 variant to the AD of the Adenoviral
353 E1A (Fig. 1b) also resulted in co-condensation with p300 (Fig. 5c; row 12). We therefore
354 conclude that, at a minimal level, both BRD4 BD acetyl-lysine binding and TF AD-mediated
355 p300 recruitment and activation are required for co-condensation.
356
357 Addition of 1,6-hexanediol, the p300/CBP HAT inhibitor A-485 or the BET inhibitor JQ1 all
358 abolished condensation of GFP-BRD4-NUTwt, mut1, mut2 and ΔNPS confirming that both
359 acetylation by p300/CBP and BRD4 BD substrate engagement are required (Fig. 5d, Table S6

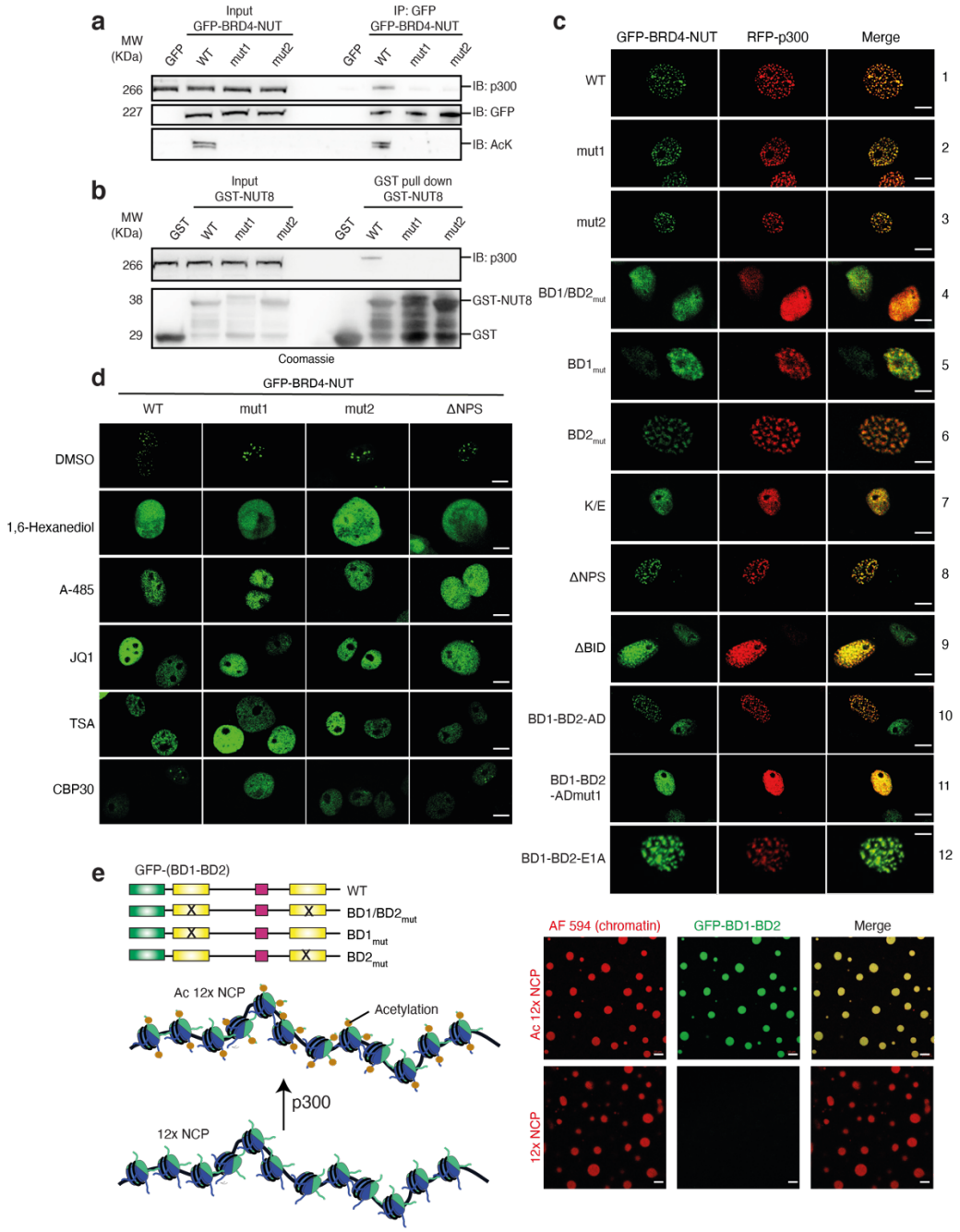


**Figure 5. Mechanism of condensation of BRD4-NUT and p300. a,** Cos7 cells were transfected with GFP-BRD4-NUT variants or GFP alone as the control. Co-immunoprecipitation (IP) experiments were performed using anti-GFP antibody and immuno-blotted (IB) for p300, GFP and Acetylated-Lysine. Input samples were loaded as a control. Experiments were independently repeated at least three times. **b,** Purified GST-NUT8 wild type and mutants 1 & 2 were incubated with Cos7 cells extract for 4 hours. The complexes were pull-down by Glutathione Sepharose beads and analysed by SDS-PAGE followed by Coomassie staining (bottom) or by IB for p300 (top). **c**, Cos7 cells were transfected with the indicated GFP-BRD4-NUT and RFP-p300 constructs and analysed by fluorescence microscopy, BRD4-NUT (green) and p300 (red). Scale bars, 10 μm. Quantification of foci formation of different BRD4-NUT variants and their co-localization with p300 are shown in Tables S4 and S5. **d**, Cos7 cells were transfected with the indicated GFP-BRD4-NUT constructs and treated with DMSO (control), 1,6-hexanediol, p300 HAT inhibitor A485, pan-BET inhibitor JQ1, HDAC inhibitor TSA or p300 bromodomain inhibitor CBP30. Scale bars, 10 μm. Quantification of foci formation in presence of CBP30 is shown in Table S6. **e**, Shematic representation of GFP-labelled BRD4 mutants and Alexa Fluor 594 labelled reconstituted chromatin containing non-acetylated (12x NCP) or acetylated (Ac 12X NCP) 12 Nucleosome Core Particles. Fluorescence microscopy images of non-acetylated or acetylated 12x NCP chromatin incubated with GFP-BD1-BD2. Scale bars, 10 μm.

360 and S7). HDAC inhibition results in expansion of Histone acetylation and retargets lysine-acetyl
361 readers including BRD4 thus partially mimicking the effect of BD inhibition[82]. In agreement
362 with this model, addition of the HDAC inhibitor Trichostatin A abolished condensation of all
363 variants (Fig. 5d). Immunofluorescence experiments further showed that the BRD4-NUT
364 condensates colocalise with HDAC1 thus confirming that these sites correspond to high
365 acetylation turnover (Fig. S5b).
366
367 As mutation of the NUT AD did not abolish p300 recruitment into the condensate we further
368 assessed the contribution of the CBP/p300 BD. We used the CBP30 inhibitor that has~34-fold
369 higher selectivity for CBP/p300 BD as compared to BRD4 BD1[83]. Addition of CBP30 did not
370 impact the condensation of GFP-BRD4-NUTwt and ΔNPS. However, condensation of the NUT
371 AD mutants GFP-BRD4-NUTmut1 and mut2 was sensitive to CBP30 treatment (Fig. 5d, Table
372 S7). Thus, the NUT AD mutants reveal that co-condensation can also occur through a p300 BD-
373 acetyl-lysine-dependent recruitment mechanism. Thus, two interactions drive BRD4-NUT and
374 p300 co-condensation: (1) interaction of p300 with the AD domain in NUT and (2) p300 BD-
375 acetyl-lysine engagement. Disruption of both interactions, but not each interaction individually,
376 abolishes the co-condensation reaction.
377
378 **Condensation requires BD multivalency**
379 Our observation that mutation of BD1 but not BD2 largely abolished BRD4-NUT condensation
380 in cells (Fig. 5c; row 5, 6) suggests that condensation in cells is not simply driven by BRD4 BD
381 divalency. We therefore tested the requirements of acetylation-dependent chromatin
382 condensation *in vitro*. Previous data show that addition of BRD4 or an engineered multivalent
383 protein containing five copies $(BD1)_5$ of BRD4 BD1 induces condensation of p300-acetylated
384 nucleosome arrays *in vitro*[58].
385
386 We generated dodecameric nucleosome arrays (Fig. 5e, Fig. S5d). In agreement with previous
387 data[58], non-acetylated nucleosome arrays formed round droplets that were dissolved by p300
388 acetylation (Fig. S5e), in agreement with the model that acetylation disrupts internucleosomal
389 interactions[84]. As expected, addition of GFP-$(BD1)_5$ allowed droplet formation of acetylated but
390 not of non-acetylated nucleosome arrays (Fig. S5f). This condensation reaction was driven by
391 acetyl-lysine binding as a N140A mutation in the BD1 acetyl-lysine binding pocket abolished
392 droplet formation (Fig. S5g).
393
394 As a minimal BRD4 construct containing BD1-BD2 (amino acids 1-459) induced condensation
395 in cells when fused to the NUT AD, we tested if BD1-BD2 divalency is sufficient to drive
396 droplet formation *in vitro*. BRD4 BD1-BD2 enabled droplet formation of acetylated but not of
397 non-acetylated nucleosome arrays (Fig. 5e, right) in the same way as the GFP-$(BD1)_5$. Mutation
398 of the BD acetyl-lysine binding pockets individually or in combination abolished droplet
399 formation (Fig. S5g). We conclude that the BD divalency of BRD4 is sufficient to drive
400 condensation *in vitro*. As large-scale condensation in cells is sensitive to BD1 but not BD2
401 mutation (Fig. 5c), our model is that BRD4 oligomerisation contributes to condensation.
402
403 **Dynamics of condensation of BRD4-NUT and p300**
404 Time-lapse imaging showed that the condensates remained stable during the experiment (Fig. 6a,
405 Movie S2). Addition of 1,6-hexanediol resulted in rapid and transient dissolution of the

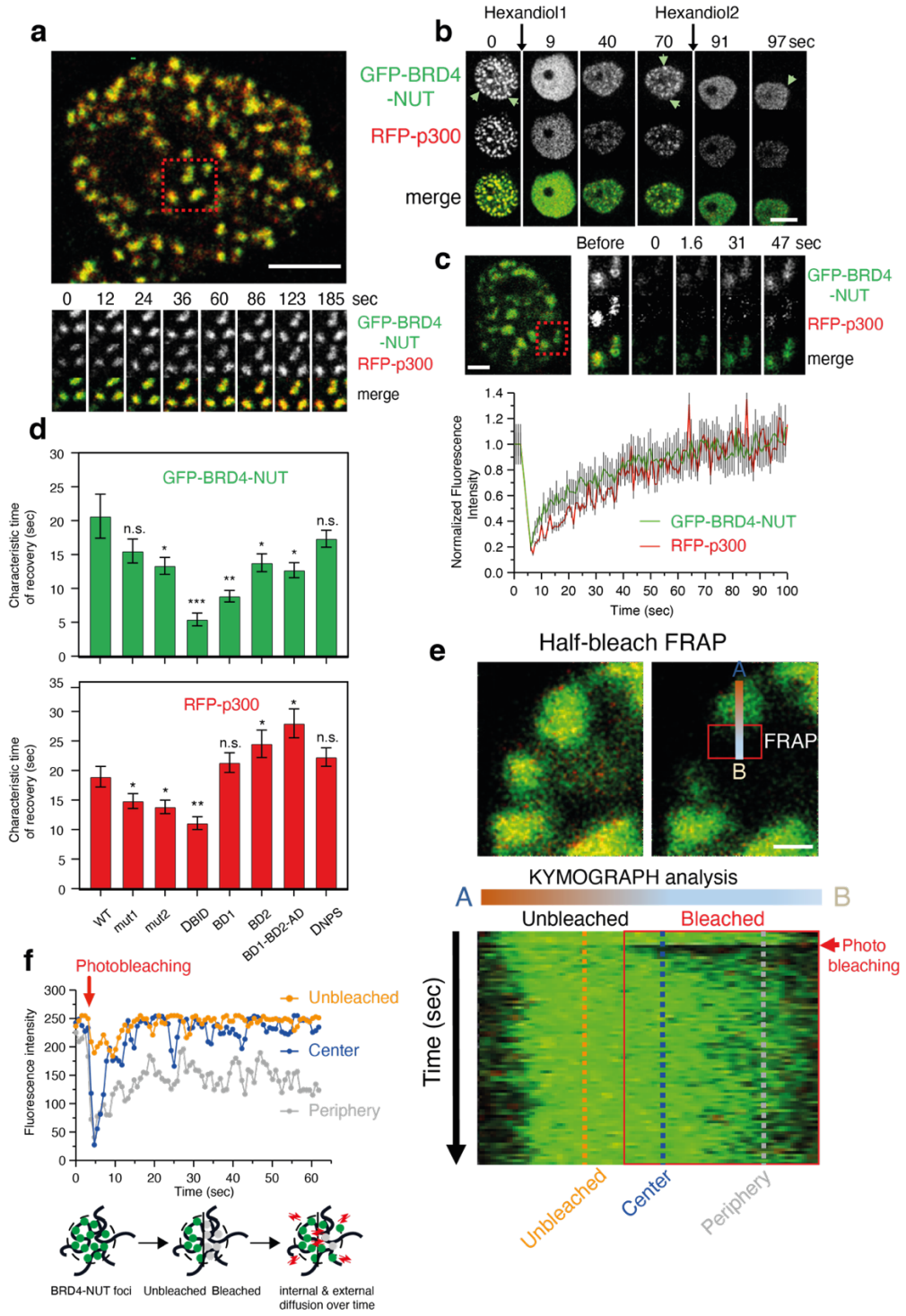


**Figure 6. Dynamics of condensation of BRD4-NUT and p300. a,** Example image of nuclear droplets. Red square: Time laps imaging of BRD4-NUT and p300 droplets; Scale bar, 4 µm. **b,** Time laps imaging after addition of 3% [w/v] 1,6 Hexanediol. Scale bar, 12 µm. **c**, Top: Example image of droplets (red square) after photobleaching. Scale bar, 2 µm. Bottom: Quantification of the FRAP experiments. 3 independent technical replicates were done. Averages and standard error of mean (SEM; grey bars) are shown. **d**, Quantification of the characteristic time of recovery rates for different GFP-BRD4-NUT mutants (top) and RFP-p300 (bottom). Three to four technical replicate FRAP experiments were done for each mutant (40 to 65 foci measured). Data shown are mean +/- standard error of mean (SEM). Statistical differences in recovery rates were determined by Student's t-test. *p≤0.05; **p≤0.01; ***p≤0.001; n.s. non-significant difference as compared to WT. **e**, Half-bleach FRAP experiment. Top: The area before (left) and after (right) laser bleach are shown. The red box indicates the bleached area. Scale bar, 0.5 µm. Bottom: The change in fluorescence intensity along the A-B axis was analysed in the Kymograph. **f**, Top: Plot of fluorescence recovery from the Kymograph for the unbleached area, center and periphery of the droplet. Bottom: cartoon of the internal and external exchange.

406 condensate (Fig. 6b). After reformation, a second addition of 1,6-hexanediol dissolved the
407 condensates again illustrating their dynamic and transient nature. To study the consequences of
408 the BRD4-NUT mutations on turnover of the condensate we performed Fluorescence Recovery
409 After Photobleaching (FRAP) experiments. Wild-type GFP-BRD4-NUT and RFP-p300
410 recovered ~50% of signal after ~20 sec (Fig. 6c). Thus, while droplets appear stable at the
411 mesoscale, the molecules are highly mobile at the nanoscale and in constant exchange with the
412 nucleoplasm. Mutation of BRD4-NUT mostly interfered with droplet retention as shown by
413 increased FRAP recovery rates (Fig. 6d). p300 dynamics was directly coupled to that of the
414 BRD4-NUT mutants except for the GFP-BRD4-NUT BD2 and the BD1-BD2-AD constructs
415 which showed slower p300 recovery rates indicating some degree of functional uncoupling.
416
417 To assay internal droplet dynamics, we performed half-bleach FRAP experiments (Fig. 6e). We
418 analysed the change in fluorescence intensity over time along a defined A-B axis in the bleached
419 (red square) and unbleached area. Kymograph analysis showed that the fluorescence signal in the
420 'unbleached' region (orange line) and the droplet 'center' (blue line) recovered much quicker
421 and to completion as compared to the 'periphery' of the droplet (grey line), which only partially
422 recovered signal (Fig. 6f). Our interpretation is that recovery at the center occurs more quickly
423 because high local concentration in the droplet centre maintains a feed-forward acetylation
424 reaction that traps quickly diffusing molecules. At the droplet periphery, lower concentrations
425 and competition with HDACs destabilizes droplet assembly leading to reduced recovery rates.
426 As there is (1) constant exchange with the nucleoplasm and (2) no preferential equilibration
427 between the bleached and unbleached area we argue that these condensates are 'liquid'-like at
428 the nanoscale but not at the mesoscale where the viscoelastic properties of the 'solid' chromatin
429 scaffold constrain dynamic exchange[85]. As a result, we do not see droplet fission or fusion at
430 least during the time-course of our experiments.
431
432 **Discussion**
433 Chromatin acetylation has long been linked to transcriptional activation, by altering chromatin
434 structure and by enabling binding of BD containing proteins[86-88]. How acetylation promotes
435 transcription has remained elusive. p300 is responsible for up to a third of nuclear acetylation[35].
436 The BRD4-NUT fusion reveals how constitutive activation of p300 establishes a self-organizing,
437 acetylation-dependent feed-forward reaction that results in large-scale intra- and
438 interchromosomal interactions with an oncogenic outcome[62]. In addition to its well-known role
439 in enhancer function and control of gene expression[32,49], p300 is also involved in
440 compartmentalisation of the genome into eu- and heterochromatin[33]. We argue that key aspects
441 of these reactions involve modulation of an acetylation-dependent condensation reaction we
442 describe here.
443
444 Regulation of p300 is central for establishment of an acetylation-dependent condensation
445 reaction (Fig. 7a). We propose that in the deacetylated state p300 is auto-inhibited by the RING,
446 TAZ2 domains and the AIL. p300 is activated by trans-autoacetylation[47,89,90]. Due to low p300
447 concentration[34], self-collision and activation do not occur spontaneously. Instead, as HDACs are
448 estimated to be ~100-fold more abundant[34], p300 most frequently collides with HDAC
449 complexes[91,92] which maintain p300 in the inactive conformation. In this inactive state p300 is
450 evenly dispersed in the nucleus[47].
451

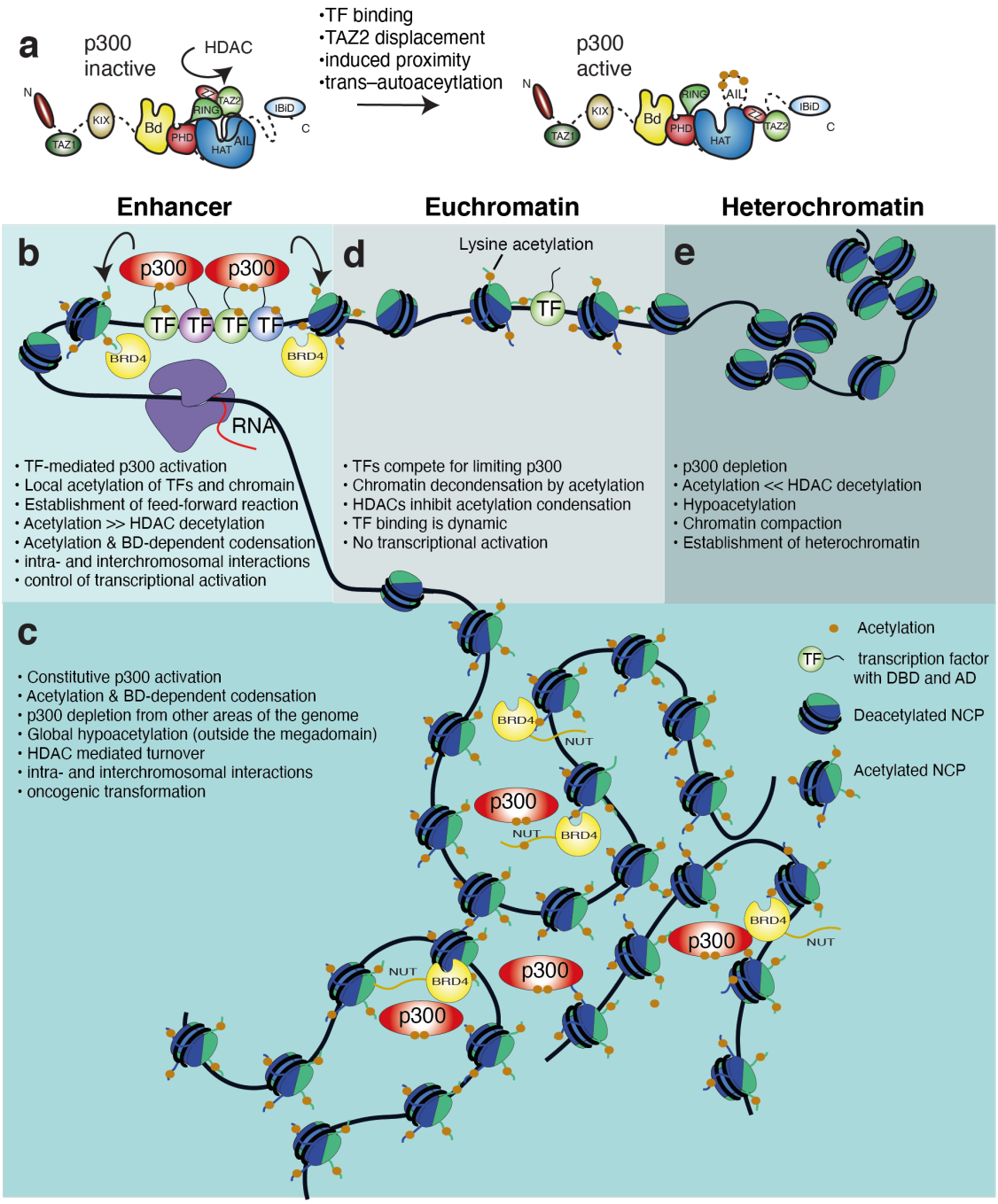


**Figure 7. Molecular model for p300 activation in physiological setting and disease**. **a**, p300 is maintained in the inactive state by HDACs. Activation requires TF binding which results autoacetylation and removal of autoinhibition. **b,** In enhancer signalling, TFs interact through their ADs with the different protein interaction domains of p300 which results in scaffolding of dynamic TF assemblies. Local TF and histone acetylation allows binding of BD containing proteins including BRD4 thus establishing positive feed-back. HDACs are located in these condensates and enable dynamic turnover thus resulting in bistability and response to changes in TF signaling. **c,** In BRD4-NUT NMC, the acetylation-dependent reaction drives formation of intra- and interchromosomal interactions resulting in the formation of a Megadomain. **d,** TF binding and acetylation establish open Euchromatin. TFs compete for limiting p300 co-activators but TF-DNA binding outside enhancer clusters remains transient and, due to high HDAC activity, does not effectively establish an acetylation-dependent condensate. **e,** Depletion and partitioning of p300 into euchromatic compartments results in hypoacetylation due to high HDAC activity. Hypoacetylated compartments become a substrate for heterochromatinization.

452 Induced proximity, by TF binding, enables p300 self-collision, trans-autoacetylation and
453 activation[47]. The BRD4-NUT system reveals an autoinhibitory role for the TAZ2 domain which
454 is relieved upon NUT AD binding (Fig. 4). Accordingly, the well-characterized TAZ2 ligand
455 E1A[93,94] also stimulates p300 auto- and substrate acetylation (Fig. 4), as also reported for other
456 TAZ2 ligands[95,96]. Thus, we propose that the TAZ2 domain plays a role in allosteric HAT
457 regulation: TF AD binding results in displacement of the TAZ2 domain from its auto-inhibitory
458 position resulting in HAT activation thus directly coupling TF AD-mediated p300 binding to
459 HAT activation.
460
461 Perturbation of the autoinhibitory function of the RING and TAZ2 domains by mutation all lead
462 to constitutive p300 activation and condensation reactions similar to what is seen with BRD4-
463 NUT[44,47]. Importantly, comprehensive studies of cancer cell lines show that truncation of the
464 TAZ2 domain (Fig. S4k) leads to p300 HAT gain-of-function in disease[78,79]. An acetylation-
465 dependent condensation reaction may also explain how Adenoviral E1A causes genome-wide
466 relocalisation of p300 and activation of genes that promote cell growth and division[97-99]. Not
467 unlike BRD4-NUT, this condensation reaction is also sensitive to p300 HAT, BD and HDAC
468 inhibition[99]. Therefore, while p300 is thought of as a classic tumor suppressor, with loss of
469 function mutations occurring in a number of different cancers[100], constitutive activation by
470 mutation or by interaction with activating ligands such as BRD4-NUT and E1A can lead to
471 acetylation-dependent condensation with an oncogenic outcome.
472
473 As numerous TFs interact with p300 trough their ADs[31,45], we predict that the condensation
474 reaction establishes intra- and interchromosomal interactions that are normally involved in
475 enhancer signaling (Fig. 7b). Many TF ADs, including NUT (Fig. 1), are IDRs that form
476 dynamic interactions with the different protein interaction domains of p300[75,101-110]. Due to such
477 multivalent AD interactions, p300 is able to scaffold TF assembly on complex enhancer elements
478 thereby facilitating combinatorial control of enhancer-mediated transcription[111-113].
479
480 TF-mediated recruitment and activation of p300 result in local histone and TF acetylation and
481 establishment of positive feed-back through binding by BD containing proteins. High rates of
482 self-collision of p300 maintain this positive feedback and establish a self-organizing feed-
483 forward reaction resulting in co-condensation of p300, BET proteins BRD2, BRD3, and BRD4
484 and numerous transcriptional and chromatin regulators[66]. The condensation reaction is limited by
485 HDACs which are usually present at active enhancers and promoters[114,115], and prevent
486 hyperacetylation and transcriptional inhibition[116,117]. HDAC1 is localised in the BRD4-NUT
487 condensate (Fig. S5b). Our FRAP experiments show that the condensates are 'liquid'-like at the
488 nanoscale and we propose that HDACs enable continuous and dynamic turnover. If the feed-
489 forward condensation reaction is sufficiently strong, it will overcome this inhibitory effect by
490 HDACs provided that local high concentrations are maintained. As a result, the BRD4-NUT
491 condensate is essentially stable at the mesoscale despite continuous internal dynamic exchange.
492 In enhancer signaling, this dynamic bistability may then render the condensate more immediately
493 responsive to dynamic and transient changes in TF signaling and explain the short transcriptional
494 burst kinetics seen in cells[118,119].
495
496 The reaction redistributes p300 (and BD containing proteins) into the condensate thus leading to
497 depletion from other genomic regions (Fig. 5)[63]. The condensation reaction thus leads to high

498 local acetylation (in the condensate) but global histone hypoacetylation elsewhere[120].
499 Counterintuitively, treatment with HDAC inhibitors does not lead to BRD4-NUT
500 'hypercondensation'. Instead, HDACi restores global histone acetylation[120] and rapidly dissolves
501 the BRD4-NUT/p300 condensate (Fig. 5). In agreement with recent data[82], our model is that
502 HDAC inhibition and resultant increased global histone acetylation redistributes BD containing
503 proteins thereby decreasing their effective local concentration resulting in droplet dissolution.
504 Due to the diffusible nature of the reactants, maintenance of global histone hypoacetylation is
505 therefore a key aspect of how such condensates arise. We therefore argue that HDACs contribute
506 to transcriptional regulation by maintaining (1) dynamic bistability of enhancer condensates and
507 (2) global hypoacetylation which in turn 'enables' focal enhancer condensation. Thus, the dual
508 nature of HDAC function with roles in gene activation and repression[114,121-123] would then be
509 directly linked to modulation of these condensation reactions.
510
511 While histone H3K27 acetylation has long been seen as a signature mark for active
512 enhancers[124,125], p300 also acetylates numerous non-histone substrates including many TFs[35].
513 Therefore, we do not see a role for a defined 'code' in how such modifications contribute to the
514 signalling reaction[126]. Instead, promiscuous lysine acetylation of TFs and histones drive
515 emergent multivalency that kinetically traps diffusing BD-domain containing factors such as
516 p300 and BRD4. While individual BDs typically have weak binding affinity and specificity[127],
517 local proximity facilitates rebinding after dissociation thus enabling an acetylation-dependent
518 feed-forward co-condensation reaction (Fig. 6). We propose that this biophysical mechanism
519 enables formation of an 'exploratory' network of interactions that generates bistability by
520 positive feedback and enables focal accumulation of regulatory factors on enhancers and
521 establishment of long-range interactions that control promoter activity[119]. Successful
522 establishment of this 'exploratory' network could then explain the long-standing observation that
523 multiple TF DNA binding sites synergistically activate transcription without the requirement of
524 physical interaction between TFs[112,128].
525
526 It has long-been known that TFs activate some genes while at the same time repressing others
527 through competitive coactivator 'squelching'[30,129-135]. Accordingly, in BRD4-NUT, the
528 sequestration of p300 inhibits p53 and the apoptotic cell response while knock-down of BRD4-
529 NUT releases p300, and restores p53-dependent cell differentiation and apoptosis[63]. Thus, we
530 predict that competition for diffusible co-activators and successful establishment of a continual
531 acetylation-dependent condensation reaction is a key regulatory control mechanism: only
532 enhancers containing the appropriate set of clustered TF binding sites will effectively compete
533 and establish such an acetylation-dependent condensate. As TFs locate their target DNA sites
534 using 'facilitated diffusion'[136,137], we propose that following TF-DNA binding, the combined
535 action of p300 scaffolding, TF acetylation and formation of an acetylation-dependent condensate
536 slows down the dynamic search behaviour thus increasing local concentration, residency time
537 and transcription activation. Accordingly, acetylation-mediated increase of TF residence time has
538 been described for p53[138,139] and could thus control TF turnover and transcriptional
539 regulation[140,141].
540
541 Binding events that occur outside TF enhancer clusters are then unable to compete for limited
542 co-activators, fail to establish such an acetylation-condensation reaction and therefore remain
543 transcriptionally inactive[142-144]. Due to high concentrations of HDACs[34] and rapid deacetylation

544 kinetics across the genome[35,91], the acetylation-dependent condensation reaction is transient. It is
545 such transient and dynamic acetylation that establishes euchromatic compartments without
546 necessarily leading to transcriptional activation (Fig. 7d).
547
548 There is increasing evidence suggesting a role for LLPS of intrinsically disordered proteins in
549 different nuclear processes[39,59,60]. IDR-driven condensation reactions of chromatin-binding
550 proteins including BRD4 and p300 have been implicated in gene regulation[37-39,41,42,49,59,60] and in
551 disease[145,146]. As BRD4-NUT and p300 are largely disordered (Fig. 1; 72% and 42% predicted
552 IDR, respectively) our assumption was that IDR-mediated interactions would contribute to the
553 condensation reaction.
554
555 While the NUT AD region can indeed form spherical condensates *in vitro* as analysed by SAXS
556 (Fig. S6), we do not think that this is relevant for the condensation reaction in cells. Even a
557 minimal BRD4 BD1-BD2 construct, removing a large fraction of IDR sequence from BRD4-
558 NUT, enables condensation in cells provided it contains a functional AD (Fig. 5c). As an
559 equivalent NUT AD mutant (that fails to bind to the TAZ2 domain) does not enable the
560 condensation we exclude the possibility that residual structural disorder, e.g. the 200 amino acid
561 linker between the BD1 and BD2 domains of BRD4, drives the condensation reaction. We and
562 others have shown that the condensation reaction is inhibited by (1) the BET BD inhibitor
563 JQ1[63,67], (2) mutation of the acetyl-lysine binding pocket of BRD4 BD1 or, (3) the DNA binding
564 surfaces of BRD4 BD1/BD2 or, (4) p300 HAT inhibition (Fig. 5). *In vitro*, divalency of BD1-
565 BD2 was essential for condensation of acetylated nucleosome arrays (Fig. 5e). BET proteins are
566 thought to oligomerize[50,56] and BRD4 phosphorylation enables dimerization[147]. We propose that
567 the combination of BD divalency and BET oligomerization provide multivalency that enables
568 condensation of acetylated chromatin in cells. Several p300 HAT gain-of-function mutations,
569 that interfere with the autoinhibitory function of the RING and TAZ2 domains, enable a similar
570 acetylation- and BD-dependent condensation reactions[47]. We therefore conclude that the reaction
571 is driven by p300 activation and engagement of acetylated chromatin by the BDs. In accordance,
572 single-gene imaging data support the notion that promoter-enhancer communication and
573 transcription control depend on TF and BRD4 clustering driven by specific DNA and BD
574 binding rather than IDR-mediated interactions[61].
575
576 The co-activator depletion reaction may also be one of the key reaction mechanisms that enables
577 the physical segregation of transcriptionally active euchromatin from repressed heterochromatin
578 (Fig. 7e), and explain the general link between the transcriptional state and 3D chromatin
579 compartmentalisation[148]. Targeting of heterochromatin with acidic TF ADs or treatment with
580 HDAC inhibitors generally counteracts heterochromatinization even in the absence of active
581 transcription[17-23,149-151]. TF-mediated retention of p300 in euchromatin enables establishment of
582 heterochromatin in worms[33], while depletion of p300 and chromatin hypoacetylation facilitates
583 methylation by PRC2[91]. Thus, competition for and partitioning of limiting key acetylases by TFs
584 into euchromatin and depletion from heterochromatin, together with BD-mediated higher order
585 chromatin folding[50,51,56], may drive key aspects of 'epigenetic' genome compartmentalization.
586 Phenomena such as stochastic and exclusive choice of monoallelic gene expression or X-
587 chromosome inactivation in mammals may then also depend on depletion of limiting
588 coactivators and establishment of positive feedback so that only the 'winning' allele drives gene
589 expression while 'competing' alleles are silenced[152-156].

## References


1 Lieberman-Aiden, E. *et al.* Comprehensive mapping of long-range interactions reveals folding principles of the human genome. *Science* **326**, 289-293, doi:10.1126/science.1181369 (2009).

2 Schwarzer, W. *et al.* Two independent modes of chromatin organization revealed by cohesin removal. *Nature* **551**, 51-56, doi:10.1038/nature24281 (2017).

3 Dixon, J. R. *et al.* Topological domains in mammalian genomes identified by analysis of chromatin interactions. *Nature* **485**, 376-380, doi:10.1038/nature11082 (2012).

4 Nora, E. P. *et al.* Spatial partitioning of the regulatory landscape of the X-inactivation centre. *Nature* **485**, 381-385, doi:10.1038/nature11049 (2012).

5 Nuebler, J., Fudenberg, G., Imakaev, M., Abdennur, N. & Mirny, L. A. Chromatin organization by an interplay of loop extrusion and compartmental segregation. *Proc Natl Acad Sci U S A* **115**, E6697-E6706, doi:10.1073/pnas.1717730115 (2018).

6 Misteli, T. The Self-Organizing Genome: Principles of Genome Architecture and Function. *Cell* **183**, 28-45, doi:10.1016/j.cell.2020.09.014 (2020).

7 van de Werken, H. J. G. *et al.* Small chromosomal regions position themselves autonomously according to their chromatin class. *Genome Res* **27**, 922-933, doi:10.1101/gr.213751.116 (2017).

8 Solovei, I., Thanisch, K. & Feodorova, Y. How to rule the nucleus: divide et impera. *Curr Opin Cell Biol* **40**, 47-59, doi:10.1016/j.ceb.2016.02.014 (2016).

9 Wang, L. *et al.* Histone Modifications Regulate Chromatin Compartmentalization by Contributing to a Phase Separation Mechanism. *Mol Cell* **76**, 646-659 e646, doi:10.1016/j.molcel.2019.08.019 (2019).

10 Erdel, F. & Rippe, K. Formation of Chromatin Subcompartments by Phase Separation. *Biophys J* **114**, 2262-2270, doi:10.1016/j.bpj.2018.03.011 (2018).

11 Falk, M. *et al.* Heterochromatin drives compartmentalization of inverted and conventional nuclei. *Nature* **570**, 395-399, doi:10.1038/s41586-019-1275-3 (2019).

12 Larson, A. G. *et al.* Liquid droplet formation by HP1alpha suggests a role for phase separation in heterochromatin. *Nature* **547**, 236-240, doi:10.1038/nature22822 (2017).

13 Strom, A. R. *et al.* Phase separation drives heterochromatin domain formation. *Nature* **547**, 241-245, doi:10.1038/nature22989 (2017).

14 Erdel, F. *et al.* Mouse Heterochromatin Adopts Digital Compaction States without Showing Hallmarks of HP1-Driven Liquid-Liquid Phase Separation. *Mol Cell* **78**, 236-249 e237, doi:10.1016/j.molcel.2020.02.005 (2020).

15 Strom, A. R. *et al.* HP1alpha is a chromatin crosslinker that controls nuclear and mitotic chromosome mechanics. *Elife* **10**, doi:10.7554/eLife.63972 (2021).

16 Ho, J. W. *et al.* Comparative analysis of metazoan chromatin organization. *Nature* **512**, 449-452, doi:10.1038/nature13415 (2014).

17 Tumbar, T., Sudlow, G. & Belmont, A. S. Large-scale chromatin unfolding and remodeling induced by VP16 acidic activation domain. *J Cell Biol* **145**, 1341-1354, doi:DOI 10.1083/jcb.145.7.1341 (1999).

18 Carpenter, A. E., Memedula, S., Plutz, M. J. & Belmont, A. S. Common effects of acidic activators on large-scale chromatin structure and transcription. *Mol Cell Biol* **25**, 958-968, doi:10.1128/MCB.25.3.958-968.2005 (2005).

19 Therizols, P. *et al.* Chromatin decondensation is sufficient to alter nuclear organization in embryonic stem cells. *Science* **346**, 1238-1242, doi:10.1126/science.1259587 (2014).

20 Taddei, A., Maison, C., Roche, D. & Almouzni, G. Reversible disruption of pericentric heterochromatin and centromere function by inhibiting deacetylases. *Nat Cell Biol* **3**, 114-120, doi:10.1038/35055010 (2001).

21 Mueller, W. G., Walker, D., Hager, G. L. & McNally, J. G. Large-scale chromatin decondensation and recondensation regulated by transcription from a natural promoter. *Mol Biol Cell* **12**, 357a-357a (2001).

640 22 Toth, K. F. *et al.* Trichostatin A-induced histone acetylation causes decondensation of interphase
641 chromatin. *J Cell Sci* **117**, 4277-4287, doi:10.1242/jcs.01293 (2004).
642 23 Chambeyron, S. & Bickmore, W. A. Chromatin decondensation and nuclear reorganization of the
643 HoxB locus upon induction of transcription. *Gene Dev* **18**, 1119-1130, doi:10.1101/gad.292104
644 (2004).
645 24 Avantaggiati, M. L. *et al.* The SV40 large T antigen and adenovirus E1a oncoproteins interact
646 with distinct isoforms of the transcriptional co-activator, p300. *EMBO Journal* **15**, 2236-2248
647 (1996).
648 25 Green, M. R. Eukaryotic transcription activation: right on target. *Mol Cell* **18**, 399-402,
649 doi:10.1016/j.molcel.2005.04.017 (2005).
650 26 Malik, S. & Roeder, R. G. The metazoan Mediator co-activator complex as an integrative hub for
651 transcriptional regulation. *Nat Rev Genet* **11**, 761-772, doi:10.1038/nrg2901 (2010).
652 27 Allen, B. L. & Taatjes, D. J. The Mediator complex: a central integrator of transcription. *Nat Rev*
653 *Mol Cell Biol* **16**, 155-166, doi:10.1038/nrm3951 (2015).
654 28 Merika, M., Williams, A. J., Chen, G., Collins, T. & Thanos, D. Recruitment of CBP/p300 by the
655 IFN beta enhanceosome is required for synergistic activation of transcription. *Mol Cell* **1**, 277-
656 287 (1998).
657 29 Reiter, F., Wienerroither, S. & Stark, A. Combinatorial function of transcription factors and
658 cofactors. *Curr Opin Genet Dev* **43**, 73-81, doi:10.1016/j.gde.2016.12.007 (2017).
659 30 Kamei, Y. *et al.* A CBP integrator complex mediates transcriptional activation and AP-1
660 inhibition by nuclear receptors. *Cell* **85**, 403-414 (1996).
661 31 Goodman, R. H. & Smolik, S. CBP/p300 in cell growth, transformation, and development. *Genes*
662 *Dev* **14**, 1553-1577 (2000).
663 32 Narita, T. *et al.* Enhancers are activated by p300/CBP activity-dependent PIC assembly, RNAPII
664 recruitment, and pause release. *Mol Cell* **81**, 2166-2182 e2166, doi:10.1016/j.molcel.2021.03.008
665 (2021).
666 33 Cabianca, D. S. *et al.* Active chromatin marks drive spatial sequestration of heterochromatin in C.
667 elegans nuclei. *Nature* **569**, 734-739, doi:10.1038/s41586-019-1243-y (2019).
668 34 Gillespie, M. A. *et al.* Absolute Quantification of Transcription Factors Reveals Principles of
669 Gene Regulation in Erythropoiesis. *Mol Cell* **78**, 960-974 e911, doi:10.1016/j.molcel.2020.03.031
670 (2020).
671 35 Weinert, B. T. *et al.* Time-Resolved Analysis Reveals Rapid Dynamics and Broad Scope of the
672 CBP/p300 Acetylome. *Cell* **174**, 231-244 e212, doi:10.1016/j.cell.2018.04.033 (2018).
673 36 Hnisz, D., Shrinivas, K., Young, R. A., Chakraborty, A. K. & Sharp, P. A. A Phase Separation
674 Model for Transcriptional Control. *Cell* **169**, 13-23, doi:10.1016/j.cell.2017.02.007 (2017).
675 37 Boija, A. *et al.* Transcription Factors Activate Genes through the Phase-Separation Capacity of
676 Their Activation Domains. *Cell* **175**, 1842-1855 e1816, doi:10.1016/j.cell.2018.10.042 (2018).
677 38 Chong, S. *et al.* Imaging dynamic and selective low-complexity domain interactions that control
678 gene transcription. *Science* **361**, doi:10.1126/science.aar2555 (2018).
679 39 Sabari, B. R. *et al.* Coactivator condensation at super-enhancers links phase separation and gene
680 control. *Science* **361**, doi:10.1126/science.aar3958 (2018).
681 40 Cho, W. K. *et al.* Mediator and RNA polymerase II clusters associate in transcription-dependent
682 condensates. *Science* **361**, 412-415, doi:10.1126/science.aar4199 (2018).
683 41 Zamudio, A. V. *et al.* Mediator Condensates Localize Signaling Factors to Key Cell Identity
684 Genes. *Mol Cell* **76**, 753-766 e756, doi:10.1016/j.molcel.2019.08.016 (2019).
685 42 Guo, Y. E. *et al.* Pol II phosphorylation regulates a switch between transcriptional and splicing
686 condensates. *Nature* **572**, 543-+, doi:10.1038/s41586-019-1464-0 (2019).
687 43 Shrinivas, K. *et al.* Enhancer Features that Drive Formation of Transcriptional Condensates. *Mol*
688 *Cell* **75**, 549-561 e547, doi:10.1016/j.molcel.2019.07.009 (2019).

689 44 Delvecchio, M., Gaucher, J., Aguilar-Guerreri, C., Ortega, E. & Panne, D. Structure of the p300
690 catalytic core and implications for chromatin targeting and HAT regulation. *Nature Structural*
691 *and Molecular Biology* **21**, doi:10.1038/nsmb.2642 (2013).
692 45 Dyson, H. J. & Wright, P. E. Role of Intrinsic Protein Disorder in the Function and Interactions of
693 the Transcriptional Coactivators CREB-binding Protein (CBP) and p300. *J Biol Chem* **291**, 6714-
694 6722, doi:10.1074/jbc.R115.692020 (2016).
695 46 Dancy, B. M. & Cole, P. A. Protein lysine acetylation by p300/CBP. *Chem Rev* **115**, 2419-2452,
696 doi:10.1021/cr500452k (2015).
697 47 Ortega, E. *et al.* Transcription factor dimerization activates the p300 acetyltransferase. *Nature*
698 **562**, 538-544, doi:10.1038/s41586-018-0621-1 (2018).
699 48 Zhang, Y. *et al.* Nuclear condensates of p300 formed though the structured catalytic core can act
700 as a storage pool of p300 with reduced HAT activity. *Nat Commun* **12**, 4618,
701 doi:10.1038/s41467-021-24950-8 (2021).
702 49 Ma, L. *et al.* Co-condensation between transcription factor and coactivator p300 modulates
703 transcriptional bursting kinetics. *Mol Cell*, doi:10.1016/j.molcel.2021.01.031 (2021).
704 50 Pivot-Pajot, C. *et al.* Acetylation-dependent chromatin reorganization by BRDT, a testis-specific
705 bromodomain-containing protein. *Mol Cell Biol* **23**, 5354-5365, doi:10.1128/MCB.23.15.5354-
706 5365.2003 (2003).
707 51 Gaucher, J. *et al.* Bromodomain-dependent stage-specific male genome programming by Brdt.
708 *EMBO J* **31**, 3809-3820, doi:10.1038/emboj.2012.233 (2012).
709 52 Goudarzi, A. *et al.* Dynamic Competing Histone H4 K5K8 Acetylation and Butyrylation Are
710 Hallmarks of Highly Active Gene Promoters. *Mol Cell* **62**, 169-180,
711 doi:10.1016/j.molcel.2016.03.014 (2016).
712 53 Shiota, H. *et al.* Nut Directs p300-Dependent, Genome-Wide H4 Hyperacetylation in Male Germ
713 Cells. *Cell Rep* **24**, 3477-3487 e3476, doi:10.1016/j.celrep.2018.08.069 (2018).
714 54 Zhao, R., Nakamura, T., Fu, Y., Lazar, Z. & Spector, D. L. Gene bookmarking accelerates the
715 kinetics of post-mitotic transcriptional re-activation. *Nature Cell Biology* **13**, 1295-U1239,
716 doi:10.1038/ncb2341 (2011).
717 55 Devaiah, B. N. *et al.* BRD4 is a histone acetyltransferase that evicts nucleosomes from chromatin.
718 *Nat Struct Mol Biol* **23**, 540-548, doi:10.1038/nsmb.3228 (2016).
719 56 Wang, R., Li, Q., Helfer, C. M., Jiao, J. & You, J. Bromodomain protein Brd4 associated with
720 acetylated chromatin is important for maintenance of higher-order chromatin structure. *J Biol*
721 *Chem* **287**, 10738-10752, doi:10.1074/jbc.M111.323493 (2012).
722 57 Ladurner, A. G., Inouye, C., Jain, R. & Tjian, R. Bromodomains mediate an acetyl-histone
723 encoded antisilencing function at heterochromatin boundaries. *Molecular Cell* **11**, 365-376,
724 doi:Doi 10.1016/S1097-2765(03)00035-2 (2003).
725 58 Gibson, B. A. *et al.* Organization of Chromatin by Intrinsic and Regulated Phase Separation. *Cell*
726 **179**, 470-484 e421, doi:10.1016/j.cell.2019.08.037 (2019).
727 59 Shin, Y. *et al.* Liquid Nuclear Condensates Mechanically Sense and Restructure the Genome.
728 *Cell* **175**, 1481-1491 e1413, doi:10.1016/j.cell.2018.10.057 (2018).
729 60 Han, X. *et al.* Roles of the BRD4 short isoform in phase separation and active gene transcription.
730 *Nat Struct Mol Biol* **27**, 333-341, doi:10.1038/s41594-020-0394-8 (2020).
731 61 Li, J. *et al.* Single-gene imaging links genome topology, promoter-enhancer communication and
732 transcription control. *Nat Struct Mol Biol* **27**, 1032-1040, doi:10.1038/s41594-020-0493-6 (2020).
733 62 Eagen, K. P. & French, C. A. Supercharging BRD4 with NUT in carcinoma. *Oncogene* **40**, 1396-
734 1408, doi:10.1038/s41388-020-01625-0 (2021).
735 63 Reynoird, N. *et al.* Oncogenesis by sequestration of CBP/p300 in transcriptionally inactive
736 hyperacetylated chromatin domains. *EMBO J* **29**, 2943-2952, doi:emboj2010176 [pii]
737 10.1038/emboj.2010.176 (2010).

64 Yan, J., Diaz, J., Jiao, J., Wang, R. & You, J. Perturbation of BRD4 protein function by BRD4-NUT protein abrogates cellular differentiation in NUT midline carcinoma. *J Biol Chem* **286**, 27663-27675, doi:10.1074/jbc.M111.246975 (2011).

65 Alekseyenko, A. A. *et al.* The oncogenic BRD4-NUT chromatin regulator drives aberrant transcription within large topological domains. *Genes Dev* **29**, 1507-1523, doi:10.1101/gad.267583.115 (2015).

66 Alekseyenko, A. A. *et al.* Ectopic protein interactions within BRD4-chromatin complexes drive oncogenic megadomain formation in NUT midline carcinoma. *Proc Natl Acad Sci U S A* **114**, E4184-E4192, doi:10.1073/pnas.1702086114 (2017).

67 Wang, R. & You, J. Mechanistic analysis of the role of bromodomain-containing protein 4 (BRD4) in BRD4-NUT oncoprotein-induced transcriptional activation. *J Biol Chem* **290**, 2744-2758, doi:10.1074/jbc.M114.600759 (2015).

68 Rosencrance, C. D. *et al.* Chromatin Hyperacetylation Impacts Chromosome Folding by Forming a Nuclear Subcompartment. *Mol Cell* **78**, 112-126 e112, doi:10.1016/j.molcel.2020.03.018 (2020).

69 Staller, M. V. *et al.* A High-Throughput Mutational Scan of an Intrinsically Disordered Acidic Transcriptional Activation Domain. *Cell Syst* **6**, 444-455 e446, doi:10.1016/j.cels.2018.01.015 (2018).

70 Dominguez, C., Boelens, R. & Bonvin, A. M. HADDOCK: a protein-protein docking approach based on biochemical or biophysical information. *Journal of the American Chemical Society* **125**, 1731-1737, doi:10.1021/ja026939x (2003).

71 Basu, S. *et al.* Unblending of Transcriptional Condensates in Human Repeat Expansion Disease. *Cell* **181**, 1062-1079 e1030, doi:10.1016/j.cell.2020.04.018 (2020).

72 Plevin, M. J., Mills, M. M. & Ikura, M. The LxxLL motif: a multifunctional binding sequence in transcriptional regulation. *Trends Biochem Sci* **30**, 66-69, doi:10.1016/j.tibs.2004.12.001 (2005).

73 Evans, R. *et al.* Protein complex prediction with AlphaFold-Multimer. *bioRxiv*, doi:10.1101/2021.10.04.463034 (2021).

74 Jumper, J. *et al.* Highly accurate protein structure prediction with AlphaFold. *Nature* **596**, 583-589, doi:10.1038/s41586-021-03819-2 (2021).

75 Krois, A. S., Ferreon, J. C., Martinez-Yamout, M. A., Dyson, H. J. & Wright, P. E. Recognition of the disordered p53 transactivation domain by the transcriptional adapter zinc finger domains of CREB-binding protein. *Proc Natl Acad Sci U S A* **113**, E1853-1862, doi:10.1073/pnas.1602487113 (2016).

76 Zhang, Y. *et al.* The ZZ domain of p300 mediates specificity of the adjacent HAT domain for histone H3. *Nat Struct Mol Biol* **25**, 841-849, doi:10.1038/s41594-018-0114-9 (2018).

77 Sheahan, T. W., Major, V., Webb, K. M., Bryan, E. & Voigt, P. The TAZ2 domain of CBP/p300 directs acetylation towards H3K27 within chromatin. *bioRxiv* (2020).

78 Ghandi, M. *et al.* Next-generation characterization of the Cancer Cell Line Encyclopedia. *Nature* **569**, 503-508, doi:10.1038/s41586-019-1186-3 (2019).

79 Kumar, M. *et al.* Inhibition of histone acetyltransferase function radiosensitizes CREBBP/EP300 mutants via repression of homologous recombination, potentially targeting a gain of function. *Nat Commun* **12**, 6340, doi:10.1038/s41467-021-26570-8 (2021).

80 Miller, T. C. *et al.* A bromodomain-DNA interaction facilitates acetylation-dependent bivalent nucleosome recognition by the BET protein BRDT. *Nat Commun* **7**, 13855, doi:10.1038/ncomms13855 (2016).

81 Wu, S. Y., Lee, A. Y., Lai, H. T., Zhang, H. & Chiang, C. M. Phospho switch triggers Brd4 chromatin binding and activator recruitment for gene-specific targeting. *Mol Cell* **49**, 843-857, doi:10.1016/j.molcel.2012.12.006 (2013).

82 Slaughter, M. J. *et al.* HDAC inhibition results in widespread alteration of the histone acetylation landscape and BRD4 targeting to gene bodies. *Cell Rep* **34**, 108638, doi:10.1016/j.celrep.2020.108638 (2021).

789 83 Hammitzsch, A. *et al.* CBP30, a selective CBP/p300 bromodomain inhibitor, suppresses human
790 Th17 responses. *Proc Natl Acad Sci U S A* **112**, 10768-10773, doi:10.1073/pnas.1501956112
791 (2015).
792 84 Shogren-Knaak, M. *et al.* Histone H4-K16 acetylation controls chromatin structure and protein
793 interactions. *Science* **311**, 844-847, doi:10.1126/science.1124000 (2006).
794 85 Strickfaden, H. *et al.* Condensed Chromatin Behaves like a Solid on the Mesoscale In Vitro and
795 in Living Cells. *Cell* **183**, 1772-1784 e1713, doi:10.1016/j.cell.2020.11.027 (2020).
796 86 Dhalluin, C. *et al.* Structure and ligand of a histone acetyltransferase bromodomain. *Nature* **399**,
797 491-496, doi:10.1038/20974 (1999).
798 87 Strahl, B. D. & Allis, C. D. The language of covalent histone modifications. *Nature* **403**, 41-45,
799 doi:10.1038/47412 (2000).
800 88 Eberharter, A. & Becker, P. B. Histone acetylation: a switch between repressive and permissive
801 chromatin. Second in review series on chromatin dynamics. *EMBO Rep* **3**, 224-229,
802 doi:10.1093/embo-reports/kvf053 (2002).
803 89 Thompson, P. R. *et al.* Regulation of the p300 HAT domain via a novel activation loop. *Nat*
804 *Struct Mol Biol* **11**, 308-315, doi:10.1038/nsmb740
805 nsmb740 [pii] (2004).
806 90 Karanam, B., Jiang, L., Wang, L., Kelleher, N. L. & Cole, P. A. Kinetic and mass spectrometric
807 analysis of p300 histone acetyltransferase domain autoacetylation. *J Biol Chem* **281**, 40292-
808 40301, doi:10.1074/jbc.M608813200 (2006).
809 91 Hogg, S. J. *et al.* Targeting histone acetylation dynamics and oncogenic transcription by catalytic
810 P300/CBP inhibition. *Mol Cell* **81**, 2183-2200 e2113, doi:10.1016/j.molcel.2021.04.015 (2021).
811 92 Black, J. C., Mosley, A., Kitada, T., Washburn, M. & Carey, M. The SIRT2 deacetylase regulates
812 autoacetylation of p300. *Mol Cell* **32**, 449-455, doi:S1097-2765(08)00696-5 [pii]
813 10.1016/j.molcel.2008.09.018 (2008).
814 93 Pelka, P. *et al.* Transcriptional control by adenovirus E1A conserved region 3 via p300/CBP.
815 *Nucleic Acids Res* **37**, 1095-1106, doi:10.1093/nar/gkn1057 (2009).
816 94 Hsu, E., Pennella, M. A., Zemke, N. R., Eng, C. & Berk, A. J. Adenovirus E1A Activation
817 Domain Regulates H3 Acetylation Affecting Varied Steps in Transcription at Different Viral
818 Promoters. *J Virol* **92**, doi:10.1128/JVI.00805-18 (2018).
819 95 Kraus, W. L., Manning, E. T. & Kadonaga, J. T. Biochemical analysis of distinct activation
820 functions in p300 that enhance transcription initiation with chromatin templates. *Molecular and*
821 *Cellular Biology* **19**, 8123-8135 (1999).
822 96 Hansson, M. L. *et al.* The transcriptional coactivator MAML1 regulates p300 autoacetylation and
823 HAT activity. *Nucleic Acids Res* **37**, 2996-3006, doi:gkp163 [pii]
824 10.1093/nar/gkp163 (2009).
825 97 Ferrari, R. *et al.* Epigenetic reprogramming by adenovirus e1a. *Science* **321**, 1086-1088,
826 doi:10.1126/science.1155546 (2008).
827 98 Horwitz, G. A. *et al.* Adenovirus small e1a alters global patterns of histone modification. *Science*
828 **321**, 1084-1085, doi:10.1126/science.1155544 (2008).
829 99 Ferrari, R. *et al.* Adenovirus small E1A employs the lysine acetylases p300/CBP and tumor
830 suppressor Rb to repress select host genes and promote productive virus infection. *Cell Host*
831 *Microbe* **16**, 663-676, doi:10.1016/j.chom.2014.10.004 (2014).
832 100 Attar, N. & Kurdistani, S. K. Exploitation of EP300 and CREBBP Lysine Acetyltransferases by
833 Cancer. *Cold Spring Harb Perspect Med* **7**, doi:10.1101/cshperspect.a026534 (2017).
834 101 Wojciak, J. M., Martinez-Yamout, M. A., Dyson, H. J. & Wright, P. E. Structural basis for
835 recruitment of CBP/p300 coactivators by STAT1 and STAT2 transactivation domains. *EMBO J*
836 **28**, 948-958, doi:emboj200930 [pii]
837 10.1038/emboj.2009.30 (2009).
838 102 Ferreon, J. C., Martinez-Yamout, M. A., Dyson, H. J. & Wright, P. E. Structural basis for
839 subversion of cellular control mechanisms by the adenoviral E1A oncoprotein. *Proceedings of the*

840 *National Academy of Sciences of the United States of America* **106**, 13260-13265,
841 doi:10.1073/pnas.0906770106 (2009).
842 103 Lee, C. W., Martinez-Yamout, M. A., Dyson, H. J. & Wright, P. E. Structure of the p53
843 transactivation domain in complex with the nuclear receptor coactivator binding domain of CREB
844 binding protein. *Biochemistry* **49**, 9964-9971, doi:10.1021/bi1012996 (2010).
845 104 Mukherjee, S. P. *et al.* Analysis of the RelA:CBP/p300 interaction reveals its involvement in NF-
846 kappaB-driven transcription. *PLoS Biol* **11**, e1001647, doi:10.1371/journal.pbio.1001647 (2013).
847 105 Miller Jenkins, L. M. *et al.* Characterization of the p300 Taz2-p53 TAD2 complex and
848 comparison with the p300 Taz2-p53 TAD1 complex. *Biochemistry* **54**, 2001-2010,
849 doi:10.1021/acs.biochem.5b00044 (2015).
850 106 He, J. *et al.* Structure of p300 bound to MEF2 on DNA reveals a mechanism of enhanceosome
851 assembly. *Nucleic Acids Res* **39**, 4464-4474, doi:10.1093/nar/gkr030 (2011).
852 107 Feng, H. *et al.* Structural basis for p300 Taz2-p53 TAD1 binding and modulation by
853 phosphorylation. *Structure* **17**, 202-210, doi:10.1016/j.str.2008.12.009 (2009).
854 108 Marceau, A. H. *et al.* An order-to-disorder structural switch activates the FoxM1 transcription
855 factor. *Elife* **8**, doi:10.7554/eLife.46131 (2019).
856 109 Dames, S. A., Martinez-Yamout, M., De Guzman, R. N., Dyson, H. J. & Wright, P. E. Structural
857 basis for Hif-1 alpha /CBP recognition in the cellular hypoxic response. *Proc Natl Acad Sci U S A*
858 **99**, 5271-5276, doi:10.1073/pnas.082121399 (2002).
859 110 Wang, F. *et al.* Structures of KIX domain of CBP in complex with two FOXO3a transactivation
860 domains reveal promiscuity and plasticity in coactivator recruitment. *Proc Natl Acad Sci U S A*
861 **109**, 6078-6083, doi:10.1073/pnas.1119073109 (2012).
862 111 Chan, H. M. & La Thangue, N. B. p300/CBP proteins: HATs for transcriptional bridges and
863 scaffolds. *J Cell Sci* **114**, 2363-2373 (2001).
864 112 Panne, D., Maniatis, T. & Harrison, S. C. An atomic model of the interferon-beta enhanceosome.
865 *Cell* **129**, 1111-1123, doi:S0092-8674(07)00656-3 [pii]
866 10.1016/j.cell.2007.05.019 (2007).
867 113 Panne, D. The enhanceosome. *Curr Opin Struct Biol* **18**, 236-242, doi:S0959-440X(07)00202-3
868 [pii]
869 10.1016/j.sbi.2007.12.002 (2008).
870 114 Wang, Z. *et al.* Genome-wide mapping of HATs and HDACs reveals distinct functions in active
871 and inactive genes. *Cell* **138**, 1019-1031, doi:S0092-8674(09)00841-1 [pii]
872 10.1016/j.cell.2009.06.049 (2009).
873 115 Whyte, W. A. *et al.* Enhancer decommissioning by LSD1 during embryonic stem cell
874 differentiation. *Nature* **482**, 221-225, doi:10.1038/nature10805 (2012).
875 116 Gryder, B. E. *et al.* Histone hyperacetylation disrupts core gene regulatory architecture in
876 rhabdomyosarcoma. *Nat Genet* **51**, 1714-1722, doi:10.1038/s41588-019-0534-4 (2019).
877 117 Gryder, B. E. *et al.* Chemical genomics reveals histone deacetylases are required for core
878 regulatory transcription. *Nat Commun* **10**, 3004, doi:10.1038/s41467-019-11046-7 (2019).
879 118 Fukaya, T., Lim, B. & Levine, M. Enhancer Control of Transcriptional Bursting. *Cell* **166**, 358-
880 368, doi:10.1016/j.cell.2016.05.025 (2016).
881 119 Li, J. *et al.* Single-Molecule Nanoscopy Elucidates RNA Polymerase II Transcription at Single
882 Genes in Live Cells. *Cell* **178**, 491-506 e428, doi:10.1016/j.cell.2019.05.029 (2019).
883 120 Schwartz, B. E. *et al.* Differentiation of NUT midline carcinoma by epigenomic reprogramming.
884 *Cancer Research* **71**, 2686-2696, doi:10.1158/0008-5472.CAN-10-3513 (2011).
885 121 Rundlett, S. E. *et al.* HDA1 and RPD3 are members of distinct yeast histone deacetylase
886 complexes that regulate silencing and transcription. *Proc Natl Acad Sci U S A* **93**, 14503-14508,
887 doi:10.1073/pnas.93.25.14503 (1996).
888 122 Kidder, B. L. & Palmer, S. HDAC1 regulates pluripotency and lineage specific transcriptional
889 networks in embryonic and trophoblast stem cells. *Nucleic Acids Res* **40**, 2925-2939,
890 doi:10.1093/nar/gkr1151 (2012).

123 Vogelauer, M., Wu, J., Suka, N. & Grunstein, M. Global histone acetylation and deacetylation in yeast. *Nature* **408**, 495-498, doi:10.1038/35044127 (2000).
124 Creyghton, M. P. *et al.* Histone H3K27ac separates active from poised enhancers and predicts developmental state. *Proc Natl Acad Sci U S A* **107**, 21931-21936, doi:10.1073/pnas.1016071107 (2010).
125 Rada-Iglesias, A. *et al.* A unique chromatin signature uncovers early developmental enhancers in humans. *Nature*, doi:nature09692 [pii] 10.1038/nature09692 (2010).
126 Zhang, T., Zhang, Z., Dong, Q., Xiong, J. & Zhu, B. Histone H3K27 acetylation is dispensable for enhancer activity in mouse embryonic stem cells. *Genome Biol* **21**, 45, doi:10.1186/s13059-020-01957-w (2020).
127 Filippakopoulos, P. & Knapp, S. The bromodomain interaction module. *FEBS Lett* **586**, 2692-2704, doi:10.1016/j.febslet.2012.04.045 (2012).
128 Carey, M., Lin, Y. S., Green, M. R. & Ptashne, M. A mechanism for synergistic activation of a mammalian gene by GAL4 derivatives. *Nature* **345**, 361-364 (1990).
129 Gill, G. & Ptashne, M. Negative effect of the transcriptional activator GAL4. *Nature* **334**, 721-724, doi:10.1038/334721a0 (1988).
130 Meyer, M. E. *et al.* Steroid hormone receptors compete for factors that mediate their enhancer function. *Cell* **57**, 433-442, doi:10.1016/0092-8674(89)90918-5 (1989).
131 Triezenberg, S. J., Kingsbury, R. C. & McKnight, S. L. Functional dissection of VP16, the trans-activator of herpes simplex virus immediate early gene expression. *Genes Dev* **2**, 718-729, doi:10.1101/gad.2.6.718 (1988).
132 Hottiger, M. O., Felzien, L. K. & Nabel, G. J. Modulation of cytokine-induced HIV gene expression by competitive binding of transcription factors to the coactivator p300. *EMBO J* **17**, 3124-3134, doi:10.1093/emboj/17.11.3124 (1998).
133 De Bosscher, K., Vanden Berghe, W. & Haegeman, G. The interplay between the glucocorticoid receptor and nuclear factor-kappaB or activator protein-1: molecular mechanisms for gene repression. *Endocr Rev* **24**, 488-522, doi:10.1210/er.2002-0006 (2003).
134 Portuguez, A. S. *et al.* Gene activation and repression by the glucocorticoid receptor are mediated by sequestering Ep300 and two modes of chromatin binding. *bioRxiv* (2019).
135 Guertin, M. J., Zhang, X., Coonrod, S. A. & Hager, G. L. Transient estrogen receptor binding and p300 redistribution support a squelching mechanism for estradiol-repressed genes. *Mol Endocrinol* **28**, 1522-1533, doi:10.1210/me.2014-1130 (2014).
136 Halford, S. E. An end to 40 years of mistakes in DNA-protein association kinetics? *Biochem Soc Trans* **37**, 343-348, doi:10.1042/BST0370343 (2009).
137 Mirny, L. *et al.* How a protein searches for its site on DNA: the mechanism of facilitated diffusion. *Journal of Physics A: Mathematical and Theoretical* **42**, 434013, doi:10.1088/1751-8113/42/43/434013 (2009).
138 Loffreda, A. *et al.* Live-cell p53 single-molecule binding is modulated by C-terminal acetylation and correlates with transcriptional activity. *Nat Commun* **8**, 313, doi:10.1038/s41467-017-00398-7 (2017).
139 Luo, J. *et al.* Acetylation of p53 augments its site-specific DNA binding both in vitro and in vivo. *Proc Natl Acad Sci U S A* **101**, 2259-2264, doi:10.1073/pnas.0308762101 (2004).
140 Lickwar, C. R., Mueller, F., Hanlon, S. E., McNally, J. G. & Lieb, J. D. Genome-wide protein-DNA binding dynamics suggest a molecular clutch for transcription factor function. *Nature* **484**, 251-255, doi:10.1038/nature10985 (2012).
141 Gurdon, J. B., Javed, K., Vodnala, M. & Garrett, N. Long-term association of a transcription factor with its chromatin binding site can stabilize gene expression and cell fate commitment. *Proc Natl Acad Sci U S A* **117**, 15075-15084, doi:10.1073/pnas.2000467117 (2020).

940 142 Kribelbauer, J. F., Rastogi, C., Bussemaker, H. J. & Mann, R. S. Low-Affinity Binding Sites and
941 the Transcription Factor Specificity Paradox in Eukaryotes. *Annu Rev Cell Dev Biol* **35**, 357-379,
942 doi:10.1146/annurev-cellbio-100617-062719 (2019).
943 143 Li, X. Y. *et al.* Transcription factors bind thousands of active and inactive regions in the
944 Drosophila blastoderm. *PLoS Biol* **6**, e27, doi:10.1371/journal.pbio.0060027 (2008).
945 144 Fisher, W. W. *et al.* DNA regions bound at low occupancy by transcription factors do not drive
946 patterned reporter gene expression in Drosophila. *Proc Natl Acad Sci U S A* **109**, 21330-21335,
947 doi:10.1073/pnas.1209589110 (2012).
948 145 Boija, A., Klein, I. A. & Young, R. A. Biomolecular Condensates and Cancer. *Cancer Cell* **39**,
949 174-192, doi:10.1016/j.ccell.2020.12.003 (2021).
950 146 Ahn, J. H. *et al.* Phase separation drives aberrant chromatin looping and cancer development.
951 *Nature* **595**, 591-595, doi:10.1038/s41586-021-03662-5 (2021).
952 147 Malvezzi, F. *et al.* Phosphorylation-dependent BRD4 dimerization and implications for
953 therapeutic inhibition of BET family proteins. *Commun Biol* **4**, 1273, doi:10.1038/s42003-021-
954 02750-6 (2021).
955 148 Rowley, M. J. & Corces, V. G. Organizational principles of 3D genome architecture. *Nat Rev*
956 *Genet* **19**, 789-800, doi:10.1038/s41576-018-0060-8 (2018).
957 149 Aparicio, O. M. & Gottschling, D. E. Overcoming telomeric silencing: a trans-activator competes
958 to establish gene expression in a cell cycle-dependent way. *Genes Dev* **8**, 1133-1146,
959 doi:10.1101/gad.8.10.1133 (1994).
960 150 Tumbar, T., Belmont, A. S. & Sudlow, G. P. Targeting the VP16 acidic activation domain
961 induces chances in large-scale chromatin structure and nuclear positioning. *Mol Biol Cell* **10**,
962 281a-281a (1999).
963 151 Ahmad, K. & Henikoff, S. Modulation of a transcription factor counteracts heterochromatic gene
964 silencing in Drosophila. *Cell* **104**, 839-847, doi:10.1016/s0092-8674(01)00281-1 (2001).
965 152 Jeppesen, P. & Turner, B. M. The inactive X chromosome in female mammals is distinguished by
966 a lack of histone H4 acetylation, a cytogenetic marker for gene expression. *Cell* **74**, 281-289,
967 doi:10.1016/0092-8674(93)90419-q (1993).
968 153 Spilianakis, C. G., Lalioti, M. D., Town, T., Lee, G. R. & Flavell, R. A. Interchromosomal
969 associations between alternatively expressed loci. *Nature* **435**, 637-645, doi:10.1038/nature03574
970 (2005).
971 154 Apostolou, E. & Thanos, D. Virus Infection Induces NF-kappaB-dependent interchromosomal
972 associations mediating monoallelic IFN-beta gene expression. *Cell* **134**, 85-96,
973 doi:10.1016/j.cell.2008.05.052 (2008).
974 155 Monahan, K., Horta, A. & Lomvardas, S. LHX2- and LDB1-mediated trans interactions regulate
975 olfactory receptor choice. *Nature* **565**, 448-453, doi:10.1038/s41586-018-0845-0 (2019).
976 156 Zylicz, J. J. *et al.* The Implication of Early Chromatin Changes in X Chromosome Inactivation.
977 *Cell* **176**, 182-197 e123, doi:10.1016/j.cell.2018.11.041 (2019).
978 157 Migl, D. *et al.* Cryoelectron Microscopy Structure of a Yeast Centromeric Nucleosome at 2.7 A
979 Resolution. *Structure* **28**, 363-370 e363, doi:10.1016/j.str.2019.12.002 (2020).
980 158 Franke, D. *et al.* ATSAS 2.8: a comprehensive data analysis suite for small-angle scattering from
981 macromolecular solutions. *J Appl Crystallogr* **50**, 1212-1225, doi:10.1107/S1600576717007786
982 (2017).
983 159 Petoukhov, M. V. *et al.* New developments in the program package for small-angle scattering
984 data analysis. *J Appl Crystallogr* **45**, 342-350, doi:10.1107/S0021889812007662 (2012).
985 160 Dorigo, B., Schalch, T., Bystricky, K. & Richmond, T. J. Chromatin fiber folding: requirement
986 for the histone H4 N-terminal tail. *J Mol Biol* **327**, 85-96, doi:10.1016/s0022-2836(03)00025-1
987 (2003).
988 161 Luger, K., Rechsteiner, T. J. & Richmond, T. J. Preparation of nucleosome core particle from
989 recombinant histones. *Methods Enzymol* **304**, 3-19, doi:S0076-6879(99)04003-3 [pii] (1999).

990 162 Schumann, F. H. *et al.* Combined chemical shift changes and amino acid specific chemical shift
991 mapping of protein-protein interactions. *J Biomol NMR* **39**, 275-289, doi:10.1007/s10858-007-
992 9197-z (2007).
993 163 Maciejewski, M. W. *et al.* NMRbox: A Resource for Biomolecular NMR Computation. *Biophys J*
994 **112**, 1529-1534, doi:10.1016/j.bpj.2017.03.011 (2017).
995 164 Ozenne, V. *et al.* Flexible-meccano: a tool for the generation of explicit ensemble descriptions of
996 intrinsically disordered proteins and their associated experimental observables. *Bioinformatics* **28**,
997 1463-1470, doi:10.1093/bioinformatics/bts172 (2012).
998 165 Shen, Y. & Bax, A. Protein backbone and sidechain torsion angles predicted from NMR chemical
999 shifts using artificial neural networks. *J Biomol NMR* **56**, 227-241, doi:10.1007/s10858-013-
1000 9741-y (2013).
1001 166 Zheng, S. Q. *et al.* MotionCor2: anisotropic correction of beam-induced motion for improved
1002 cryo-electron microscopy. *Nat Methods* **14**, 331-332, doi:10.1038/nmeth.4193 (2017).
1003 167 Zhang, K. Gctf: Real-time CTF determination and correction. *Journal of Structural Biology* **193**,
1004 1-12, doi:10.1016/j.jsb.2015.11.003 (2016).
1005 168 Zivanov, J. *et al.* New tools for automated high-resolution cryo-EM structure determination in
1006 RELION-3. *Elife* **7**, doi:10.7554/eLife.42166 (2018).
1007

1008 **Methods**
1009

1010 **Constructs.** cDNA encoding residues for NUT-F1c (347-588), NUT1 (347-446), NUT2 (427-527),
1011 NUT3 (508-588), NUT4 (347-480), NUT5 (347-514), NUT6 (351-470), NUT7 (448-492) (wild type and
1012 mutants), NUT8 (424-492) (wild type and mutants), NUT9 (395-482) and p53 (1-61) were cloned into the
1013 *Nco*I/*Xho*I restriction sites of vectors pETM-30 or pETM11 (EMBL) with a tobacco etch virus (TEV)-
1014 cleavable N-terminal $His_6$ glutathione S-transferase ($His_6$-GST) tag for pETM30 or an N-terminal $His_6$-
1015 tag for pETM11. The p300 TAZ2 domain constructs (TAZ2 1723-1812, TAZ2 1723-1822, TAZ2 1723-
1016 1836) were codon optimized and cloned into the *Nco*I/*BamH*I restriction sites of pETM-11 (EMBL) with
1017 a TEV-cleavable N-terminal $His_6$-tag. Cysteines which do not participate in zinc coordination were
1018 mutated to Alanine or Serine (C1738, C1746, C1769, C1770). The CH3 domain of p300 (1660-1815) was
1019 cloned using *EcoR*I/*Xho*I restriction sites in pGEX-5X1 vector with a TEV-cleavable N-terminal
1020 glutathione S-transferase (GST) tag. p300s (324-2094) and p300 core-CH3 (1043-1828 and 1043-1817)
1021 were produced as described previously[44]. The BRD4 constructs: GFP-BD1-BD2, GFP-BD1-BD2
1022 N140A/N433A, GFP-BD1-BD2 N140A and GFP-BD1-BD2 N433A were cloned into the *Nco*I/*Xho*I
1023 restriction sites of pETM11. The vectors expressing the GFP-(Bromo)5 and the GFP-(Bromo)5 N140A
1024 were gifts from Michael Rosen lab (University of Texas Southwestern). The co-expression vector
1025 encoding the *S. cerevisiae* histones was a gift from Stephen Harrison lab (Harvard Medical school). The
1026 vector expressing the E1A protein was a gift from Andy Turnell lab (University of Birmingham). For
1027 cell-based assays, all the GFP-tagged BRD4-NUT variants, RFP-tagged NUT-F1c, NUT1, NUT2, NUT3
1028 and NUT4 and RFP tagged p300 were cloned into pEGFP-C1 vector (Clontech), HA-tagged p300
1029 constructs (WT, Δ1813-1838) were cloned into pcDNA3.1. All constructs were confirmed by DNA
1030 sequencing.
1031

1032 **Expression and purification.** Expression and purification of Flag-tagged p300s and GST-tagged p300
1033 core-CH3 constructs was done as reported previously[44,47]. All p300 TAZ2 constructs were produced as
1034 inclusion bodies in *Escherichia coli* (*E. coli)* BL21 (DE3). Cells were grown to mid-log phase (OD600 ~
1035 0.6) at 37°C in Luria Broth containing 50 µg/ml kamamycin and 200 µM $ZnSO_4$. Protein expression was
1036 induced by addition of 1 mM isopropyl-β-D-thiogalactopyranoside (IPTG) at 18°C for 16h. Uniformly
1037 $^{15}N$- and $^{15}N/^{13}C$-labelled samples were produced from cells grown in M9 minimal medium containing 50
1038 µg/ml Kanamycin, 200 µM $ZnSO_4$ and 1 g/l of $^{15}NH_4Cl$ and 2g/l $^{13}C$ glucose. Cells were harvested by
1039 centrifugation for 20 mins at 5000 g in a SLC-6000 rotor (Sorvall) and resuspended in 50 ml/L culture

1040 lysis buffer 1 (20 mM Tris-HCl pH 7.5, 300 mM NaCl, 5 µM $ZnSO_4$, 1 mM Dithiothreitol (DTT)),
1041 supplemented with EDTA-free protease inhibitors (Roche), and 10 µl of benzonase nuclease (Sigma-
1042 Aldrich). Cells were sonicated and centrifuged in a SS-34 rotor (Sorvall) for 1h at 12000 rpm. The pellet
1043 was then washed three times in the lysis buffer and the final pellet resuspended in buffer 2 (20 mM Tris
1044 pH 7.5, 300 mM NaCl, 1 mM Dithiothreitol (DTT), 6 M urea) for one hour at 4 °C on a rotating device.
1045 The protein solution was centrifuged as above and the soluble fraction applied to $Ni^{2+}$-charged IMAC
1046 Sepharose 6 FF (Cytiva) beads preequilibrated with buffer 2 containing 20 mM Imidazole. The column
1047 was washed with 20 column volumes (CVs) of buffer 2 containing 20 mM Imidazole and the bound
1048 protein eluted with the buffer 2 containing 300 mM Imidazole. The protein was refolded by dialysis
1049 overnight against buffer 3 (20 mM Tris pH 7.0, 100 mM NaCl, 200 µM $ZnSO_4$ and 2 mM DTT).
1050
1051 The refolded TAZ2 was incubated with His-tagged TEV protease (1:100 w/w) for 14-16 h at 4 °C.
1052 Subtractive Ni-NTA chromatography was used to remove the residual His-tag and TEV protease. The
1053 cleaved TAZ2 was further purified on a 5ml HiTrap SP HP cation exchange column (Cytiva)
1054 preequilibrated in buffer 4 (20 mM Tris pH 7.0, 100 mM NaCl, 5 µM $ZnSO_4$ and 1 mM Dithiothreitol
1055 (DTT)) and eluted using a 20 CV NaCl gradient. The peak containing TAZ2 was further purified using a
1056 HiLoad 16/60 Superdex 75 column (Cytiva) preequilibrated with buffer 5 (20 mM Tris pH 7.0, 300 mM
1057 NaCl, 5 µM $ZnSO_4$ and 1 mM DTT). The purified protein was concentrated using a prewashed Amicon
1058 Ultra-10 concentrator (molecular weight cut off 10 kDa; EMD Millipore), flash frozen in liquid N2 and
1059 stored in -80°C.
1060
1061 Unlabeled, $^{15}N$- and $^{15}N/^{13}C$-labelled NUT fragments were produced as insoluble inclusion bodies in *E.*
1062 *coli* and purified as described above. After Ni-NTA purification, the protein was dialyzed and refolded
1063 overnight at 4°C against 1L buffer 5 (20 mM Tris pH 7.0, 300 mM NaCl, 1 mM DTT and 10% glycerol).
1064 Refolded His-GST-NUT fusion proteins were incubated with His-tagged TEV protease (1:100 w/w) for
1065 14-16 h at 4 °C. Subtractive Ni-NTA chromatography was used to remove the residual His-GST-tag and
1066 TEV protease. The cleaved NUT proteins were applied to a 5ml HiTrap Q HP anion exchange column
1067 (Cytiva) in buffer 4 without $ZnSO_4$ and eluted in a 20 CV NaCl gradient. The peak containing NUT was
1068 further purified by gel filtration on a Superdex 75 Increase 10/300 GL column (Cytiva) equilibrated in
1069 buffer 5 without $ZnSO_4$. The final proteins were concentrated in a prewashed Amicon Ultra-15
1070 Centrifugal filter (molecular weight cut off 3 kDa; EMD Millipore), flash-frozen in liquid nitrogen and
1071 stored at -80 °C.
1072
1073 The GST-E1A amino acids 1-289 and GST-p53 AD amino acids 1-61 proteins were expressed in *E. coli*
1074 BL21 (DE3) cells. Cell pellets were resuspended and sonicated in lysis buffer (20 mM Tris-HCl pH 7.5,
1075 300 mM NaCl, 0.5 mM TCEP), supplemented with EDTA-free protease inhibitors (Roche), and 10 µl of
1076 benzonase nuclease (Sigma-Aldrich) and lysed by sonication. The lysate was clarified by centrifugation
1077 for 1h in a SS-34 rotor (Sorvall) at 12000 rpm and applied to a Glutathione Sepharose 4 Fast Flow resin
1078 according to instructions from the manufacturer (Cytiva). The resin was washed with 20 CV lysis buffer
1079 and the protein was eluted in lysis buffer containing 20 mM reduced L-Glutathione. The protein solution
1080 was then dialyzed overnight against lysis buffer to remove L-Glutathione and then applied to a 5 ml
1081 HiTrap Q HP anion exchange column (Cytiva) and further purified by gel filtration on a Superdex 75
1082 Increase 10/300 GL column (Cytiva) as previously described for the NUT fragments.
1083
1084 The BRD4 GFP-BD1-BD2, GFP-BD1-BD2 N140A/N433A, GFP-BD1-BD2 N140A and GFP-BD1-BD2
1085 N433A were all expressed in *E. coli* BL21 (DE3) cells. The cells were sonicated in lysis buffer (20 mM
1086 Tris-HCl pH 7.5, 300 mM NaCl, 0.5 mM TCEP) and the lysate was clarified as previously described for
1087 the other proteins. The clarified lysate was applied to $Ni^{2+}$ charged IMAC Sepharose 6 FF (Cytiva) beads
1088 preequilibrated with lysis buffer containing 20 mM Imidazole. The column was washed with 20 column
1089 volumes (CVs) of lysis buffer and the bound proteins eluted with the lysis buffer containing 300 mM
1090 Imidazole. Imidazole was removed by dialysis overnight against 1L lysis buffer and the proteins were

1091 loaded on a 5 ml HiTrap SP HP cation exchange column (Cytiva) as described for TAZ2 and further
1092 purified using a HiLoad 16/600 Superdex 200 column (Cytiva) preequilibrated with 20 mM Tris pH 7.0,
1093 300 mM NaCl and 1 mM DTT. The purified proteins were concentrated using a prewashed Amicon
1094 Ultra-10 concentrator (molecular weight cut off 30 kDa; EMD Millipore), flash frozen in liquid N2 and
1095 stored in -80°C.
1096
1097 The GFP-(Bromo)5 and GFP-(Bromo)5 N140A were purified as described previously[58]. The co-
1098 expressed *S. cerevisiae* histones octamer was purified as described previously[157]. NUT peptides were
1099 ordered from Proteogenix.
1100
1101 **HAT assays.** The p300 autoacetylation and substrate acetylation assays were performed using [$^{14}$C]
1102 acetyl-CoA (Perkin-Elmer). Autoacetylation of p300 was quantified by autoradiography after SDS-PAGE
1103 gel analysis. The acetylation reaction was performed for 30 minutes at 30°C in 1x HAT buffer (20 mM
1104 Tris-HCl pH 7.5, 100 mM NaCl, 1 mM DTT, 10 % glycerol and 1x Complete EDTA-free protease
1105 inhibitor (Roche)) with 2.5 µM p300s or p300 core and 50 µM [$^{14}$C] acetyl-CoA with or without
1106 increasing concentrations of the different substrates (NUT fragments, NCP, E1A). 5 µl of the reaction
1107 was quenched by addition of 2.5 µl of 3x SDS gel loading buffer followed by analysis on a 4-20% SDS-
1108 PAGE gel. The gels were stained with Quick Coomassie Stain (Generon), fixed for 30 min in enhancer
1109 solution (KODAK ENLIGHTNING Rapid Autoradiography Enhancer, Perkin Elmer) and dried for 2
1110 hours using a Bio-Rad Gel Dryer. The $^{14}$C signal was quantified using phosphor imaging (Typhoon,
1111 Cytiva).
1112
1113 ***In vitro* nucleosome acetyltransferase assays.** Nucleosome acetylation reactions were performed in 20
1114 µl volume in acetylation buffer (20 mM Tris pH 7.5, 100 mM NaCl, 1 mM DTT, 10% glycerol and
1115 complete Protease Inhibitor EDTA-free (Roche)) with 50 µM Acetyl-CoA, 2.5 µM of p300s or p300 core
1116 and 2 µM of nucleosome core particles (NCPs). Control experiments contained only NCPs and Acetyl-
1117 CoA without p300. The reactions were incubated for 30 minutes at 30°C and stopped by addition of 1x
1118 SDS loading buffer. Each condition was performed in duplicate. The samples were then analyzed by
1119 SDS-PAGE and mass spectrometry.
1120
1121 **Multi angle laser light scattering-size exclusion chromatography.** SEC-MALLS was performed at a
1122 flow rate of 0.5 ml/min on a Superdex 75 Increase 10/300 GL column equilibrated in buffer (20 mM
1123 HEPES pH7.0, 300 mM NaCl, 5 µM $ZnSO_4$, 0.5 mM TCEP). 50 µl of TAZ2, NUT4 or the TAZ2:NUT4
1124 complex at 2 mg/ml were injected onto the column and multi angle laser light scattering was recorded
1125 with a laser emitting at 690 nm using a DAWN-EOS detector (Wyatt Technology Corp). The refractive
1126 index was measured using a RI2000 detector (Schambeck SFD). The molecular weight was calculated
1127 from differential refractive index measurements across the center of the elution peaks using the Debye
1128 model for protein using ASTRA software version 6.0.5.3.
1129
1130 **Biolayer interferometry assay.** BLI measurements were performed with a ForteBio Octet RED384
1131 instrument and ForteBio biosensors. Data analyses was done using ForteBio Data Analysis 9.0 software.
1132 Kinetics assays were carried out at 25 °C using settings of Standard Kinetics Acquisition rate (5.0 Hz,
1133 averaging by 20) at a sample plate shake speed of 1000 rpm. The GST-tagged NUT8 wild type and
1134 mutants were loaded onto Anti-GST biosensors and the TAZ2 protein was used as an analyte. The GST-
1135 NUT-loaded Anti-GST biosensors were dipped in kinetic buffer (1x PBS, 0.1% BSA, 0.02 % Tween 20)
1136 to establish a baseline time course and then dipped into wells containing TAZ2 (1723-1836) at various
1137 concentrations diluted in the same kinetic buffer to monitor NUT-TAZ2 binding. The dissociation step
1138 was monitored by dipping the biosensors back into the wells used to collect the baseline time course. To
1139 monitor binding due to nonspecific interactions of TAZ2 with the biosensors, Anti-GST biosensors were
1140 used as controls for every analyte concentration and a double referencing method was used for data

1141 subtraction and analysis. The subtracted binding curves were analysed and plotted as a steady-state
1142 response to obtain the dissociation constant $K_d$ value.
1143
1144 **Limited proteolysis.** To identify stable variants of NUT we performed limited proteolysis by Trypsin and
1145 Chymotrypsin. 100µl of the purified CH3-NUT-F1c complex (250 µg) and TAZ2-NUT4 complex (250
1146 µg) were incubated at 4 °C with Trypsin or Chymotrypsin with a ratio of 1:100 (w/w). At the indicated
1147 time points (30 min, 2 hours, overnight), 30 µl of the reaction was quenched by addition of 15 µl of 3x
1148 SDS gel loading buffer followed by analysis on 4-20 % SDS-PAGE gel. The stable fragments on gel were
1149 analysed by acid hydrolysis and mass spectrometry at the Proteomics Core Facility (EMBL, Heidelberg).
1150
1151 **SAXS analysis.** X-ray scattering data were collected on the NUT-F1c sample at 100 µM in phase
1152 separation buffer: 20 mM Tris pH 7.0, 2 mM DTT, 125 mM NaCl and 10% (w/v) PEG 6000 at the B21
1153 BioSAXS beamline of the Diamond Light Source (Chilton, Oxfordshire, UK). The data were analysed
1154 with the ATSAS package[158]. Data collected from the sample were substracted from buffer scattering. $R_g$
1155 values were obtained from the Guinier approximation $sR_g < 1.3$ using Primus[159]. Distance distribution
1156 functions p(r) were computed from the entire scattering curve using GNOM[159].
1157
1158 ***In vitro* NUT phase separation assay.** Phase separation of purified GST-NUT-F1c *in vitro* was done
1159 phase separation buffer. The concentrations of GST-NUT-F1c used were 0-200 µM. A GST control was
1160 used in the same concentration range under identical conditions. The droplets were visually observed and
1161 turbidity of the sample ($OD_{600}$) quantified using NanoDrop (Thermo scientific).
1162
1163 **GST pulldowns.** For GST pulldowns, 50 µg of GST-tagged NUT constructs were mixed at an equimolar
1164 concentration with binding partners in 50 µl pulldown buffer (20 mM HEPES pH 8.0, 300 mM NaCl, 0.5
1165 mM TCEP, 5µM $ZnSO_4$, 0.1% Triton X-100) containing 25 µl of a 50 % slurry of GST Sepharose 4 Fast
1166 Flow beads (Cytiva) per reaction. Reactions were incubated for 30 min at 4 °C. Twenty-five microliters
1167 of the reaction were withdrawn as the reaction input and the remainder was washed 5 times with 500 µl of
1168 pulldown buffer. Samples were boiled in 1x sample loading buffer for 5 min and analysed by SDS-
1169 PAGE.
1170
1171 **Luciferase reporter assays.** Cos7 cells were co-transfected for 36 hours with β-Galactosidase reporter
1172 plasmid and UAS-promoter luciferase reporter plasmid either alone or with GAL4 DNA binding domain
1173 (DBD) plasmid or increasing amount of GAL4-DBD-NUT-F1c plasmid. Cells were then washed and
1174 incubated 15 min at RT with Luciferase lysis buffer (1% Triton X-100, 10% Glycerol, 2 mM EDTA, 25
1175 mM Tris-HCl pH 7.8). Luciferase activity was measured directly after mixing 10µl of cellular extract
1176 with 50 µl of Luciferase substrate (Luciferase assay kit, Stratagene). Normalization was made by
1177 measuring the β-Gal activity after 1-hour incubation of 7.5 µl of cellular extract with 50 µl of β-Gal
1178 substrate (β-Gal detection kit II, Clontech).
1179
1180 **Proteomics of histone modifications.** For the identification and quantification of histone acetylation
1181 following *in vitro* HAT assays, we followed the previously published procedure[52,53]. In brief, reconstituted
1182 NCPs were incubated with 100µM acetyl-CoA, as well as purified p300s (340-2,094) or the p300 core
1183 domain (1,043-1,666) for 30 min at 30°C. HPLC-MS/MS was used to quantify site specific H2A, H2B,
1184 H3 and H4 acetylation by label-free quantification. The peak area of each histone peptide was then
1185 normalized. Two technical replicate experiments were done.
1186
1187 **Isolation and Purification of 1x601 Widom DNA.** Carrier plasmids of 1x Widom 601 repeats were
1188 purified using QIAGEN Plasmid Giga kit from 6L LB culture according to the manufacturer's
1189 instructions. 1x arrays DNA were cut from carrier plasmid DNA by incubation overnight with 5,000 units
1190 of *EcoR*V-HF restriction endonuclease (New England Biolabs) in 1x CutSmart Buffer (20 mM Tris,OAc,

1191 pH 7.9, 50 mM KOAc, 10 mM $Mg[OAc]_2$, 0.1 mg/mL BSA). The excised DNA fragments were
1192 separated from the linearized plasmid by PEG precipitation. 0.192 volume of NaCl and 8% PEG 6000
1193 were added to the DNA sample and incubated for 1h on ice, the sample was then centrifuged for 20 min
1194 at 4 °C, 27000 g. the *EcoR*V fragments contained in the supernatant were precipitated by the addition of
1195 2.5 volumes of 100% cold ethanol. The DNA fragments were air dried for 10 min and dissolved in buffer
1196 TE (10 mM Tris/HCl, pH 8.0, 1 mM EDTA). Purity of the extracted 12x601 and 1x601 fragments were
1197 verified on 0.7% agarose gels and the concentration measured by 260 nm absorbance on a NanoDrop
1198 spectrophotometer (Thermo Scientific).
1199
1200 **Isolation and Purification of 12x Widom 601 Array DNA.** 12x601 DNA template was prepared as
1201 described previously[160]. In short, 12-mer DNA with177 bp repeats of the 601 sequence separated
1202 from the rest of the plasmid by *Eco*RV sites were expressed in *E.coli* strain DH5a. The DNA was
1203 then extracted by alkaline lysis and purified on a Sepharose-6 column. The DNA template was
1204 separated from the plasmid by *EcoR*V-HF digestion and PEG6000 precipitation.
1205
1206 **Histones octamer preparation.** Wild type human histones (H2A, H2B, H3 and H4) and the cysteine
1207 mutant Xenopus H4 S47C were individually expressed in *E. coli* strain Rosetta 2 DE3 pLysS and purified
1208 following the protocol described[161], but using a RESOURCE S 6 ml cation exchange chromatography
1209 column. For octamer reconstitution, equimolar ratios of the four histones were refolded together in the
1210 presence of 5 mM β-mercaptoethanol. The octamer was then separated from dimers by gel filtration using
1211 a Superdex 200 column (Cytiva). Two batches of octamers have been generated: one fully wild-type
1212 human octamer (unlabelled octamer) and an octamer formed by wild-type human H2A, H2B, H3 and
1213 Alexa Fluor™ 594 C5 Maleimide labelled *Xenopus* H4 S47C (labelled octamer).
1214
1215 **Fluorescent labelling of histones.** The *Xenopus* H4 S47C mutant histone was labelled using Alexa
1216 Fluor™ 594 C5 Maleimide following the protocol from[58]. In short, lyophilised H4 S47C was resuspended
1217 in 7M urea, 500mM Tris-HCl pH 8 and incubated with Tris-neutralized TCEP to a final concentration of
1218 2 mM for 1 hr and 30 min at RT. Alexa Fluor™ 594 C5 Maleimide stock solution was added dropwise to
1219 a 1.5 molar excess and the mix was incubated for 4 hr at RT in the dark. The reaction was quenched by
1220 the addition of β-mercaptoethanol. The histone was then purified from the free dye by ion exchange
1221 chromatography using a HiTrap SP HP cation exchange column followed by dialysis into ultra-pure water
1222 with 5 mM β-mercaptoethanol.
1223
1224 **Mononucleosome assembly.** DNA and *Saccharomyces cerevisiae* histones octamer were mixed in a
1225 1:0.5 molar ratio. Nucleosomes were reconstituted by salt gradient dialysis method and dialysed against
1226 buffer 20 mM Tris-HCl, pH 8.0, 1 mM EDTA, 1 mM DTT with continuous decrease of NaCl
1227 concentrations (1.5, 1, 0.6 and 0.25 M) at 4 °C, 3h each dialysis step with the third dialysis step
1228 proceeding overnight using mini dialysis units (10,000 Da MWCO, Pierce Slide-a-lyzer). The
1229 reconstituted nucleosomes were quality controlled by electrophoretic mobility shift assays on 5%
1230 acrylamide native gels with 0.25x TBE running buffer.
1231
1232 **12x Nucleosome array assembly, acetylation and phase separation.** Chromatin was reconstituted *in*
1233 *vitro* by assembling the 12-mer DNA with histone octamers by step-wise salt dialysis as described
1234 previously[160], but using KCl instead of NaCl. The optimal octamer to DNA ratio was determined
1235 empirically. A mix of labelled and unlabelled histone octamer was used. The ratio of labelled to
1236 unlabelled histone octamer was also determined empirically. The reconstituted 12-mer nucleosome arrays
1237 were quality controlled by *Sca*I restriction enzyme digestion to isolate single nucleosome particles and by
1238 electrophoretic mobility shift assays on 2% agarose gel in 0.5x TBE
1239 12x601 nucleosome arrays at 2 μM mono-nucleosome concentration were incubated with 1 μM of the
1240 p300 core domain in Acetylation buffer (20 mM Tris-HCl pH 7.0, 100 mM NaCl, 10% glycerol, 1 mM

1241 DTT) for 30 min at 30 °C. The non-acetylated chromatin reactions were incubated under identical
1242 conditions but without p300 core enzyme. After acetylation, 5 μM BRD4 GFP-Bromo$_5$, GFP-Bromo$_5$
1243 N140A, 10 μM GFP-BD1-BD2, 10 μM GFP-BD1-BD2 N140A, 10 μM GFP-BD1-BD2 N433A or 10
1244 μM GFP-BD1-BD2 N140A/N433A were added to nucleosomal arrays for a final concentration of 1 μM
1245 mono-nucleosome in phase separation buffer (25 mM Tris, pH7.5, 150 mM KOAc, 1 mM MgOAc, 5%
1246 glycerol, 5 mM DTT, 0.1 mM EDTA, 0.1 mg/mL BSA)[58].
1247
1248 **Microscopy of chromatin droplets.** For confocal microscopy image acquisition, a Zeiss LSM 980
1249 Airyscan 2 microscope equipped with a Plan-Apochromat 63x/1.40 Oil DIC f/ELYRA and ZEN Blue 3
1250 acquisition and analysis software was used. Samples were imaged in 384 well glass bottom plates for
1251 microscopy which were prepared as described in[58]. In short, microscopy plates were washed with 5%
1252 Hellmanex, etched with 1 M NaOH and treated with 25 mg/mL 5K mPEG-silane. Prior to use, individual
1253 wells were passivated by incubation with freshly prepared 100 mg/mL BSA.
1254
1255 **Cross-linking mass spectrometry.** Purified solutions of both NCPs and p300 core-CH3 (1043-1828)
1256 were diluted to a concentration between 0.5 and 1 mg/ml in 20 mM HEPES pH 7.0, 300 mM NaCl, 1 mM
1257 DTT and 5 μM $ZnCl_2$ and cross linked using a homobifunctional, isotopically-coded crosslinker
1258 DiSuccinimidyl Suberate DSS-H12/D12 (Creative Molecules Inc.) at a concentration of 2 mM for 30 min
1259 at 35°C 600 rpm. The cross-linking reaction was then quenched with 0.1 volumes of 1M Ammonium
1260 bicarbonate for 10 min at 35 °C 600 rpm. The sample was then treated with 0.8 volumes of 10 M urea and
1261 250 mM Ammonium bicarbonate as well as 0.05 volumes RapiGest SF Surfactant (Waters, cat. No.
1262 186008090) and sonicated for 1 min in an ultrasound bath. DTT was later added with a final
1263 concentration of 10 mM, incubated for 30 min at 37 °C and freshly prepared Iodoacetamide was added to
1264 a final concentration of 15 mM and incubated for 30 min at room temperature in the dark. The protein
1265 was sequentially digested with Endoproteinase Lys-C and Trypsin. The enzymes were added at an
1266 enzyme to substrate ratio of 1:100 for LysC and 1:50 for Trypsin and the reaction incubated for 3-4 h at
1267 37°C. The reaction was started by LysC followed by Trypsin addition after 4h. After digestion, the
1268 sample was acidified with Trifluoroacetic acid (1% v/v final concentration) at 37°C for 30 min, spun
1269 down at 17,000 g for 5 min and the peptides were fractionated by peptide size-exclusion chromatography.
1270 The mass spectrometry experiment and cross-links identification were performed by the EMBL
1271 Proteomics core facility.
1272
1273 **Immunofluorescence and drug treatment.** Cos7 cells were seeded in glass coverslips (Lab-Tek), and
1274 GFP and RFP bearing constructs were transfected by Lipofectamine 2000. Twenty-four hours later, cells
1275 were washed with PBS and fixed with 4% paraformaldehyde for 15 min, followed by permeabilization
1276 with 0.2% Triton-X100 and 1 × PBS for 10 min at room temperature. After being blocked with 5% dry
1277 milk, 0.2% Tween 20, and 1 × PBS at RT for 30 min, slides were incubated with anti-acH4 antibody
1278 (1:100 dilution, Millipore) or anti-HDAC1 antibody (1:100 dilution, Cell Signaling Technology) in 1%
1279 dry milk, 0.1% Tween 20, and 1 × PBS in a humidified chamber at 4°C overnight and then washed three
1280 times for 5 min each in the antibody dilution buffer. The secondary antibodies were diluted at 1:500 in the
1281 same buffer and incubated in a humidified chamber for 30 min at 37°C, and then washed as for the
1282 primary antibodies. The DNA was counterstained by DAPI, and the slides were mounted in Dako
1283 fluorescent mounting medium. For the drug treatment assays, twenty-four hours after being transfected
1284 with GFP and RFP bearing constructs, Cos7 cells were treated with DMSO (Sigma), 1,6-hexanediol
1285 (10%, 1 hour, Sigma), A485 (3 μM, 1 hour, Selleck), JQ1 (1 μM, 1 hour, Selleck), TSA (0.3 μM, 12
1286 hours, Selleck) or CBP30 (1 μM, 1 hour, Selleck), then the cells were washed with PBS and fixed with
1287 4% paraformaldehyde for 15 min.
1288
1289 **Co-immunoprecipitation.** Cell pellets were lysed in 300 mM NaCl buffer (20 mM HEPES-KOH pH 7.9,
1290 300 mM NaCl, 3 mM $MgCl_2$, 0.1% NP-40, 1X protease inhibitor cocktail (Roche), 1X phosphatase

1291 inhibitor cocktail-1 (Sigma) and 10 mM sodium butyrate) for 30 min at 4 °C with rotation. After a 15 min
1292 centrifugation at 12,000g at 4°C, the supernatants were collected and separated into input and
1293 immunoprecipitate (IP) lysates. IP lysates were mixed with GFP-selector (pre-washed with 300 mM NaCl
1294 buffer three times, NanoTag) and rotated overnight at 4 °C. After washing with 300 mM NaCl buffer, IPs
1295 were released by adding Laemmli sample buffer to beads and boiling for 5 min at 100°C.
1296
1297 **Fluorescence recovery after photobleaching (FRAP).** Live imaging and fluorescence recovery after
1298 photobleaching experiments (FRAP) were performed with the LSM710 Confocor3 confocal microscope
1299 (Carl Zeiss), equipped with the Plan-Apochromat C 63X /1.4 oil-immersion objective. FRAP area, time
1300 and time interval (1 image every 783ms) were maintained identical between the different BRD4-NUT
1301 mutants and repeat measurements (N=3-4, 45 to 65 foci measured per conditions) in order to photobleach
1302 3-6 foci at the same time. To compare recovery kinetics against BRD4-NUT wild-type, FRAP
1303 measurements were fitted to a single exponential curve, $I_{(t)}=I_{(0)} + k_1e^{-k2t}$ (performed with ZEN software;
1304 Carl Zeiss Microscopy) to determine the characteristic time of recovery. Values of τ (1/ k2) were
1305 compiled and statistical significance was tested using the Student's t-test (Excel).

1306 **NMR experiments and AlphaFold calculations.** Backbone resonances of both proteins free in solution
1307 were assigned by measuring HNCO, HNCA, and HN(CO)CA spectra on $^{15}$N,$^{13}$C-labelled samples at 600
1308 (NUT7) and 700 (TAZ2) MHz. We were able to assign 87% (95%) of the NH pairs, 72% (82%) of the
1309 CO resonances and 88% (96%) of the CA resonances in the backbone of NUT7 (TAZ2).
1310
1311 Side-chain resonances of both proteins free in solution were assigned by measuring HBHA(CO)NH,
1312 H(CCO)NH, and CC(CO)NH spectra on $^{15}$N,$^{13}$C-labelled samples at 600 (NUT7) and 700 (TAZ2) MHz.
1313 We were able to assign 70% (55%) of the HA resonances, 57% (45%) of the HB resonances, and 45%
1314 (53%) of the CB resonances in NUT7 (TAZ2), as well as part of the γ-protons.
1315
1316 To determine the binding site of NUT7 on TAZ2, we measured $^{1}$H-$^{15}$N HSQC spectra on $^{15}$N-labelled
1317 TAZ2 before and after adding unlabelled NUT7. For each of the assigned peaks in the spectra we
1318 calculate the chemical shift perturbations (CSP) defined as

1319 $$CSP = \sqrt{\frac{1}{2}(\Delta\delta_H^2 + (0.14 \cdot \Delta\delta_N^2)^2)},$$

1320 in which $\Delta\delta_H^2$ and $\Delta\delta_N^2$ are the chemical shift differences upon adding NUT7 in the $^{1}$H and $^{15}$N dimensions,
1321 respectively. We used the procedure described by Schumann et al.[162] to determine whether measured
1322 CSPs are significant or not. We used the same approach to map the binding site on NUT7 monitoring a
1323 titration of a solution of $^{15}$N-labelled NUT7 with unlabelled TAZ2 using $^{1}$H-$^{15}$N HSQC spectra.
1324
1325 Both $^{13}$C- and $^{15}$N-HSQC-NOESY spectra on a sample of $^{15}$N,$^{13}$C-labelled TAZ2 to which one equivalent
1326 of unlabelled NUT7 was added and $^{15}$N-HSQC-NOESY spectra on $^{15}$N-labelled NUT7 in admixture with
1327 one equivalent of unlabelled TAZ2 were measured using standard pulse sequences. All NOESY spectra
1328 were measured at 950 MHz with a mixing time of 100 ms. The AlphaFold computational models
1329 shown in Fig. 3e and Fig. 4a were obtained from alphafold.ebi.ac.uk. Models shown in Fig. 3f
1330 and Fig. 4b were calculated using AlphaFold v2.1.1 with multimer model v1 weights[73].
1331
1332 **HADDOCK docking.** We used the HADDOCK protocol[70] with experimental information from titrations
1333 and NOESY spectra to derive a structural model of the interaction. We used the NMRbox platform[163] to
1334 carry out the calculations. In a first step, we used the results of the titration experiments to derive
1335 ambiguous distance restraints (AIRs) describing the binding interface, and we used these AIRs as input
1336 for HADDOCK to dock extended conformations of NUT7 on the TAZ2 structure derived from PDB
1337 2mzd. The best 200 structures resulting from the calculations were clustered based on the fraction of

1338 common contacts (FCC). The resulting clusters were sorted according to their agreement with the AIRs.
1339 Structures in the best cluster display the interaction of residues P448-E454 in NUT7 with TAZ2. Thus,
1340 we used the Flexible-Meccano algorithm[164] to generate an ensemble of 100 conformers of NUT7, in
1341 which the conformation of residues P448-E454 is the same as in the structure resulted from the
1342 HADDOCK calculation, whereas the rest of the chain behaves like a statistical coil. Then, we used
1343 HADDOCK again to dock this ensemble of structures on the same TAZ2 conformation as above. In this
1344 run, in addition to the same AIRs as in the preliminary run, we used distance restraints derived from
1345 NOESY spectra between S1726 in TAZ2 and residues L463 and A464 in NUT7. We also used TALOS-
1346 N[165] to derive restraints on the backbone dihedral angles of residues P448-E454 from chemical shift
1347 values. We repeated this calculation ten times with different initial seeds and velocities. Finally, the best
1348 200 structures from each of the ten runs were clustered based on the FCC. The resulting clusters were
1349 sorted according to their agreement with the AIRs and NOE-based restraints. Then, from the best-ranked
1350 cluster in each of the runs, we selected the structure with the best HADDOCK score (which is a linear
1351 combination of various energy terms and buried surface area), thereby obtaining a final set of 10
1352 structures.
1353
1354 **Cryo-electron microscopy grid preparation, data collection and image processing**
1355 Quantifoil R1.2/1.3 Au 300 grids were glow discharged for 5 min at 40 mA on a Quorum Gloqube glow-
1356 discharge unit prior to application of the sample. 3 µl of 1 µM final concentration of the mononucleosome
1357 particles in buffer 20 mM Tris-HCl, pH8.0, 250 mM NaCl, 1 mM EDTA, 1 mM DTT were applied to the
1358 grid, blotted for 3 s at blot force 10 and plunge frozen into liquid ethane using a Vitrobot Mark IV (FEI
1359 Thermo Fisher), which was set at 4°C and 100% humidity. Cryo-EM data was collected on a Thermo
1360 Fisher Scientific Titan Krios G3 transmission electron microscope at the LISCB at the University of
1361 Leicester. Electron micrographs were recorded using a K3 direct electron detector (Gatan Inc.) at a dose
1362 rate of 15 $e^-$/pix/sec and a calibrated pixel size 1.086 Å. Focusing was performed over a range between -
1363 2.3 and -1.1 µm in 0.3 µm intervals. Image processing of the NCPs was performed as follows: movie
1364 stacks were corrected for beam-induced motion and then integrated using MotionCor2[166]. All frames were
1365 retained and a patch alignment of 4 x 4 was used. Contrast transfer function (CTF) parameters for each
1366 micrograph were estimated by Gctf[167]. Integrated movies were inspected with Relion-3.1 for further
1367 image processing (243 movies). Initial particle sets were picked manually, extracted, and subjected to 2D
1368 classification in Relion 3.1[168]. Resulting classes corresponding to protein complexes were subsequently
1369 employed as references for auto-picking in Relion 3.1. Particle extraction was carried out from
1370 micrographs using a box size of 128 pixels (pixel size: 1.08 Å/pixel). An initial dataset of 80764 particles
1371 was cleaned by several iterations of 2D classification, classes exhibiting clear secondary structure features
1372 were selected for 3D classification. After iterative rounds of 3D classifications, well defined classes were
1373 selected and global refinement was performed.
1374

**Acknowledgements** We thank Christos Savva and TJ Ragan for CryoEM support. We thank Nathan Cowieson from the B21 BioSAXS beamline of the Diamond Light Source; Yingming Zhao and Jinjun Gao for mass spectroscopy analysis; Luke Bailey, Sarah Northall and Dipti Vashi for help with histone preparations. Michael K. Rosen for plasmids encoding GFP-$(Bomo)_5$ and GFP-$(Bromo)_5$ N140A; Stephen M. Hinshaw and Stephen C. Harrison for plasmids encoding *S. cerevisiae* histones; Andrew Flaus for *H. sapiens* histones; Timothy J. Richmond for histone H4 mutant plasmids; Andy Turnell for E1A plasmids. Work in the S.K. laboratory was supported by ANR Episperm4 program, by Plan Cancer Pitcher, by MSD Avenir ERICAN programs, by the Cancer ITMO (Multi-Organisation Thematic Institute) of the French Alliance for Life Sciences and Health (AVIESAN) MIC program, by the "Université Grenoble Alpes" ANR-15-IDEX-02 SYMER and LIFE programs and by Fondation ARC program RF20190208471. Work in the T.S. laboratory was supported by the BBSRC (BB/S019510/1; BB/R016275/1). Work in the D.P. laboratory was supported by grants from the Worldwide Cancer Research [16-0280], the Wellcome Trust [221881/Z/20/Z], Instruct-ERIC [PID: 18571] and the Medical Research Council [MR/W001667/1].

**Author contributions** Z.I. designed and performed most experiments, analysed and validated the data with support by L.F. T.W., O.D., N.H., C.C. and N.R performed cell biology experiments. N.S. performed NMR experiments. A.R performed chromatin analyses *in vitro*. Y. Z. and J. G. performed mass spectroscopy analysis. T.S., M.B., and S.K. provided supervision, funding acquisition and commented on the draft. D.P. was involved in conceptualization, supervision, project administration, funding acquisition. Z.I and D.P. wrote the original and revised drafts with input from all authors.

**Competing interests**: Y. Z. is a founder, board member, advisor to, and inventor on patents licensed to PTM Biolabs Inc (Hangzhou, China and Chicago, IL) and Maponos Therapeutics Inc. (Chicago, IL). The other authors declare no competing interests.

# Supplemental Figures

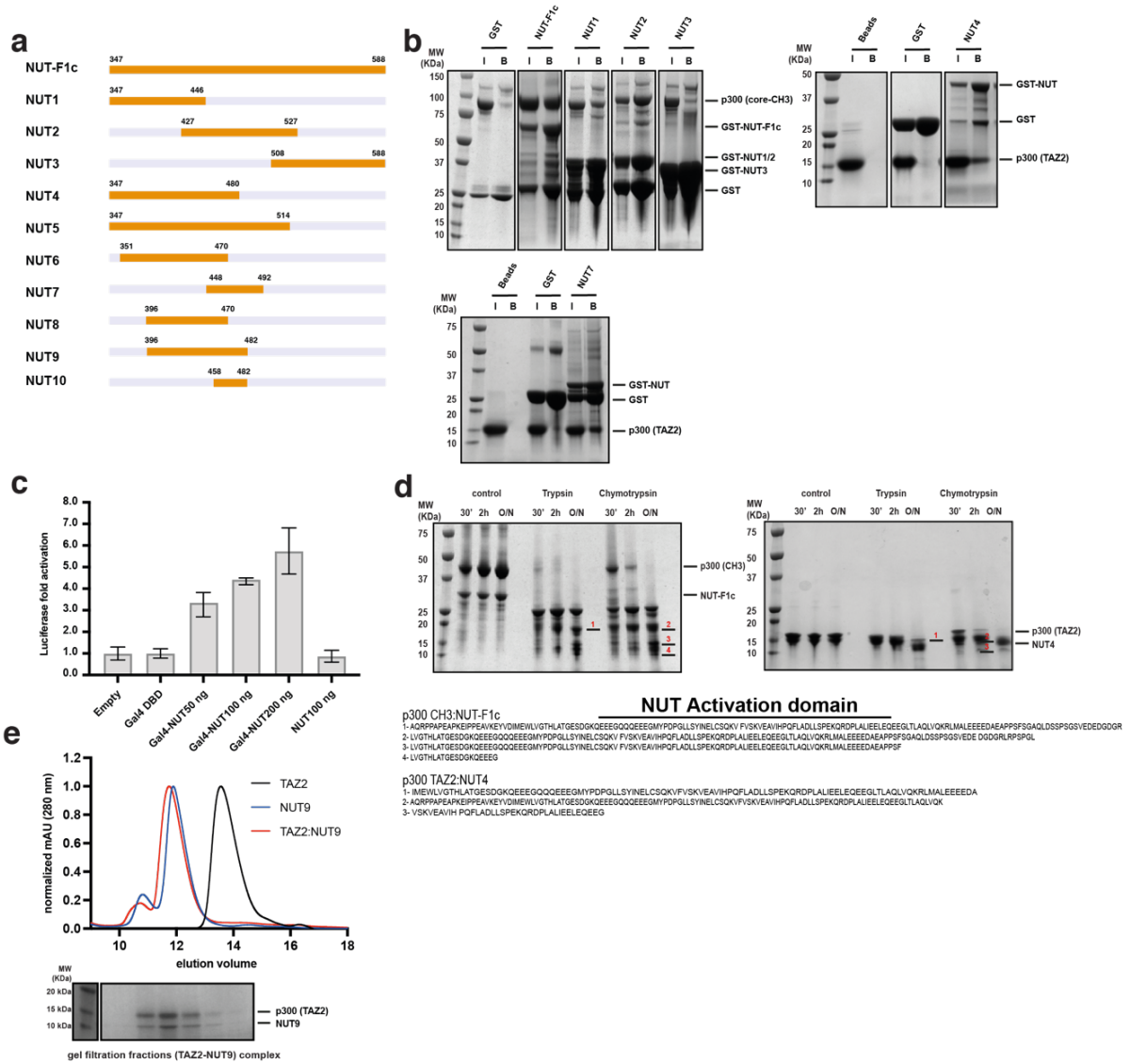


**Figure S1. Identification of an acidic activation domain in NUT. a,** Schematic of the different NUT constructs used. Sequence coordinates correspond to NUTM1 (UNIPROT Q86Y26). **b**, GST pulldown analysis between the p300 core-CH3 or the isolated TAZ2 domain and different NUT fragments. **c**, Luciferase reporter assay: Cos7 cells were co-transfected with a luciferase reporter plasmid and 'empty' plasmid, or containing the Gal4 DNA binding domain (DBD) or increasing amounts of Gal4-NUT-F1c plasmid or NUT-F1c lacking the Gal4 DBD. Luciferase expression was measured by luminescence (Luciferase assay kit, Stratagene) (right). Error bars represent standard deviations of 3 independent technical replicate experiments. **d**, Limited proteolysis of the p300 CH3-NUT-F1c complex (left) or the p300 TAZ2-NUT4 complex (right). After overnight incubation with Trypsin or Chymotrypsin samples were analysed by SDS-PAGE followed by mass spectrometry. The identified NUT fragments are highlighted on the gels and their corresponding sequences are shown on the bottom. Position of the NUT AD is indicated **e**, SEC analysis of the p300 TAZ2 domain (black), NUT9 (396-482) (blue) or the TAZ2:NUT9 complex (red) on a Superdex 75 Increase 10/300 GL column. Bottom: SDS-PAGE analysis of the peak fractions of the TAZ2-NUT9 complex.

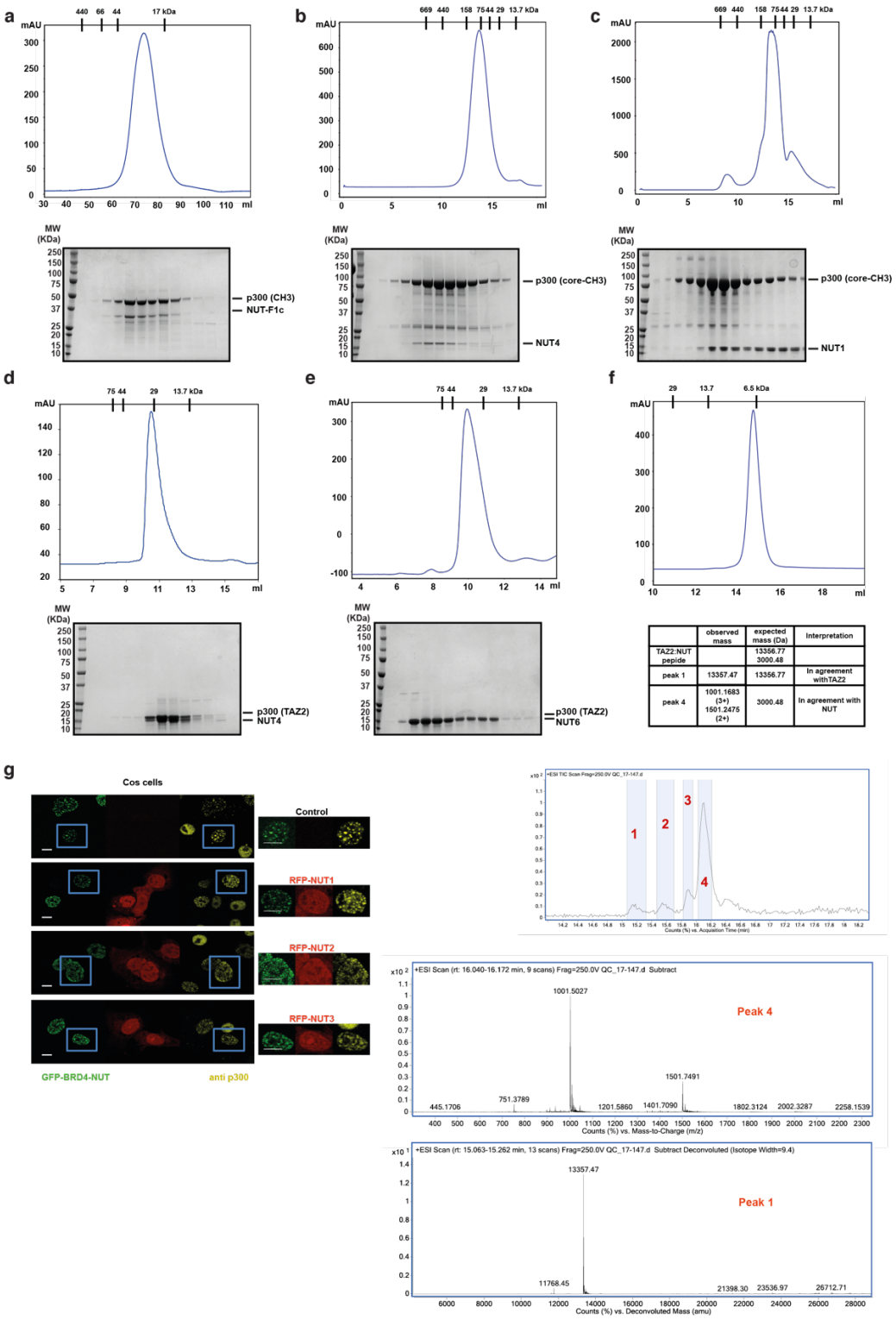


| | observed mass | expected mass (Da) | Interpretation |
|---|---|---|---|
| TAZ2:NUT pepide | | 13356.77<br>3000.48 | |
| peak 1 | 13357.47 | 13356.77 | In agreement withTAZ2 |
| peak 4 | 1001.1683 (3+)<br>1501.2475 (2+) | 3000.48 | In agreement with NUT |

**Figure S2. Identification of an acidic activation domain in NUT. a,** Size-exclusion chromatography (SEC) analysis of p300 CH3-NUT-F1c complex on HiLoad Superdex 200 column. **b**, SEC analysis of p300 core-CH3-NUT4 complex on Superdex 200 Increase 10/300. **c**, p300 core-CH3-NUT1 complex on Superdex 200 increase 10/300 GL. **d**, p300 TAZ2-NUT4 complex on Superdex 75 increase 10/300 GL. **e**, p300 TAZ2-NUT6 complex on Superdex 75 increase 10/300 GL. Bottom of each panel: SDS-PAGE analysis of the peak fractions. **f**, SEC analysis of the TAZ2-NUT10 complex on Superdex 75 increase 10/300 GL column (top). Bottom: Reverse-Phase HPLC analysis of TAZ2-NUT10 peptide complex fractions followed by electrospray ionisation time of flight mass spectrometry (LC-ESI-TOF-MS). Table: Summary of the mass spectrometry analysis data showing the presence of TAZ2 (peak 1) and the NUT peptide (peak 4). **g**, Competition analysis: Cos7 cells were transfected with constructs expressing GFP-BRD4-NUT (green) alone or co-transfected with RFP-NUT1, 2 or 3 (red). Immunofluorescence with anti-p300 antibody was used to visualize condensation of endogenous p300.

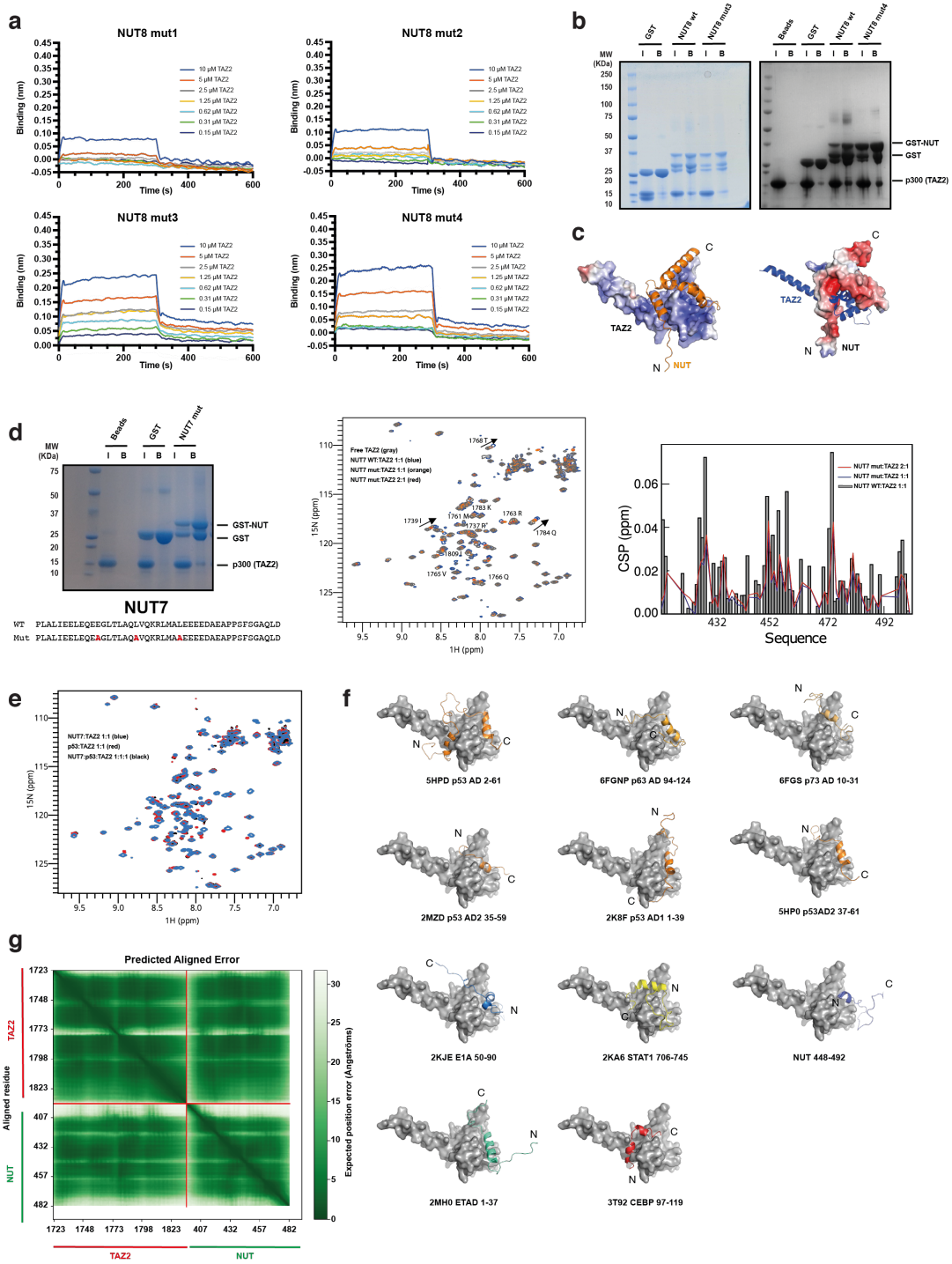


**Figure S3. Analysis of the TAZ2-NUT interaction. a,** Representative Biolayer Interferometry (BLI) profiles of p300 TAZ2 interaction with NUT8 (396-470) mutants 1, 2, 3 and 4 from which the steady-state data shown in Fig. 3b were derived. The GST-NUT8 construct was immobilized on the biosensors and TAZ2 was used as analyte and titrated at the indicated concentrations. **b,** GST pulldown analysis of TAZ2 and NUT8 (396-470) wild type and mutants 3 and 4. **c,** AlphaFold model of the TAZ2-NUT complex surface rendered and coloured according to electrostatic potential. **d,** (Left) GST pulldown analysis of TAZ2 and NUT7 (448-492) mutant. Sequences of the NUT (448-492) wild type and mutant are shown below. (Middle) $^{1}$H-$^{15}$N HSQC spectrum of free TAZ2 (gray) compared to a 1:1 molar ratio admixture with NUT7 (blue) or 1:1 (orange) and 2:1 (red) admixtures with the NUT7 mutant. (Right) Chemical shift perturbations (CSPs) upon adding 1 equimolar amount of NUT7 wild type (gray bars) to TAZ2 or after adding 1 (blue) and 2 (red) molar equivalents of the NUT7 mutant. **e,** $^{1}$H-$^{15}$N HSQC spectra of TAZ2 when 1 equivalent of NUT7 wild type (blue), p53 TAD (1-61) (red) and both NUT7 and p53 (black) are added. **f,** Overview of different TF ADs in complex with the TAZ2 domain. The N – and C-termini of the TF ADs are indicated. **g**, Predicted Aligned Error of the TAZ2-NUT AlphaFold model. The colour at position (x,y) indicates AlphaFold's expected position error at residue x, when the predicted and true structures are aligned on residue y.

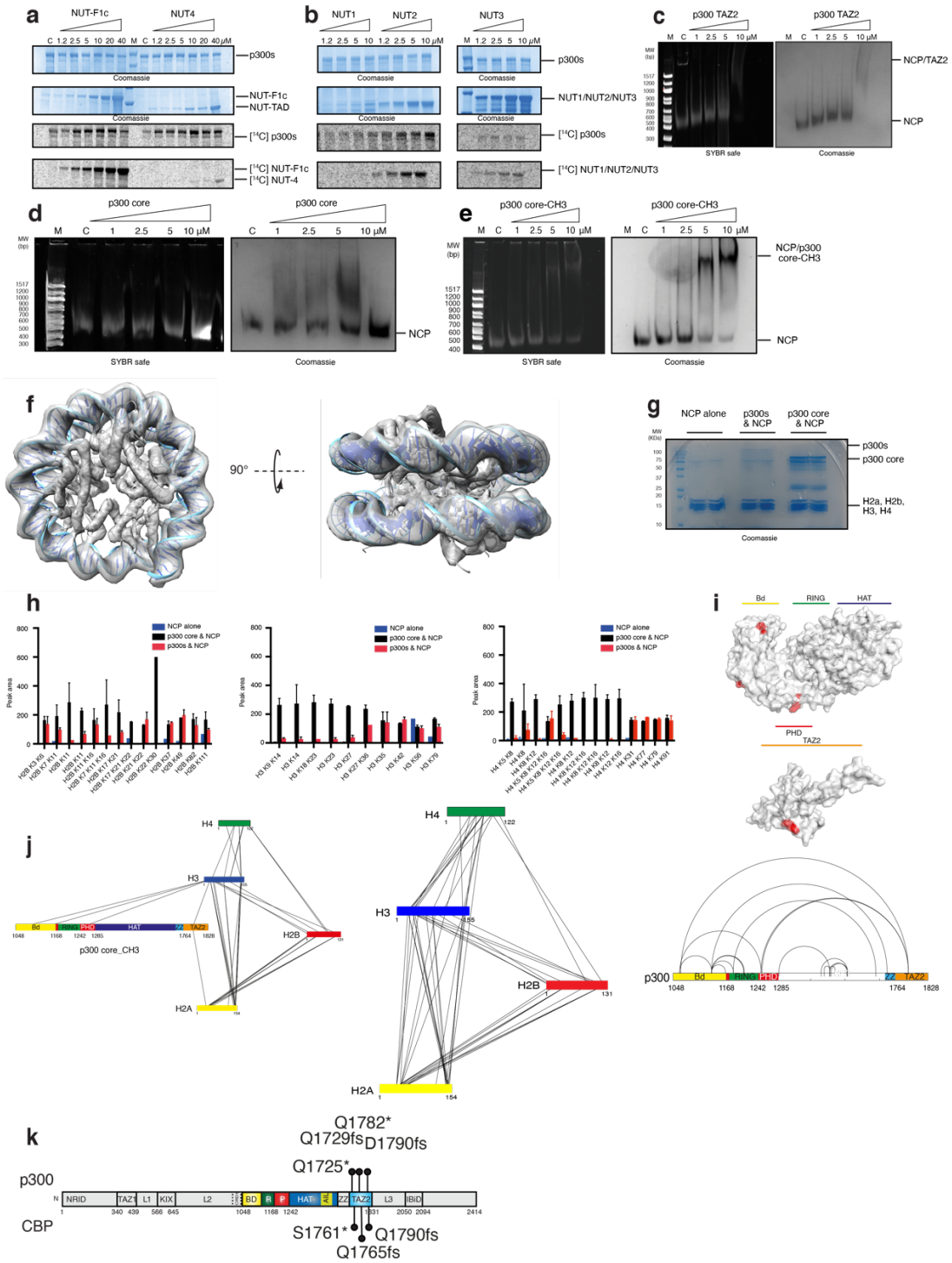


**Figure S4. Role of the TAZ2 domain in p300 regulation and substrate acetylation. a,** p300s was incubated with [$^{14}$C]Acetyl-CoA in the presence or absence (C: p300s alone) of (**a**) NUT-F1c or NUT4, **b**, NUT1, NUT2, NUT3. Samples were analysed by SDS-PAGE followed by Coomassie staining and $^{14}$C phosphor imaging. Representative data of three independent experiments are shown. **c,** EMSA analysis of NCP binding of the p300 TAZ2 domain. **d**, NCP binding of p300 core. **e**, NCP binding of p300 core-CH3. Native PAGE gels were stained with SybrSafe DNA stain or Coomassie Blue. **f,** CryoEM density for the NCP used in biochemical studies. An atomic model of the NCP (PDBs: 3LZ0) is docked into the density. **g**, SDS-PAGE gel showing input material used for quantitative mass spectrometry experiments. **h,** Quantitative mass spectrometry of NCP acetylation. Reconstituted NCPs were incubated with Acetyl-CoA and p300s or the p300 core. Quantification of the site-specific histone H2B, H3 and H4 acetylation by label-free HPLC/MS/MS. Error bars represent standard deviations from two independent technical replicate experiments. **i,** Cross-link (XL-MS) analysis of the p300 core-CH3:NCP complex. p300 residues that cross-link to the NCP histones are shown in red on p300 core (4BHW) and TAZ2 (3IO2) structures. **j**, Graphical representation of the p300:histone and histones intermolecular cross-links and intra-p300 core-CH3 cross-links. **k**, p300 (top) and CBP (bottom) gain--of-function mutations in the TAZ2 domain.

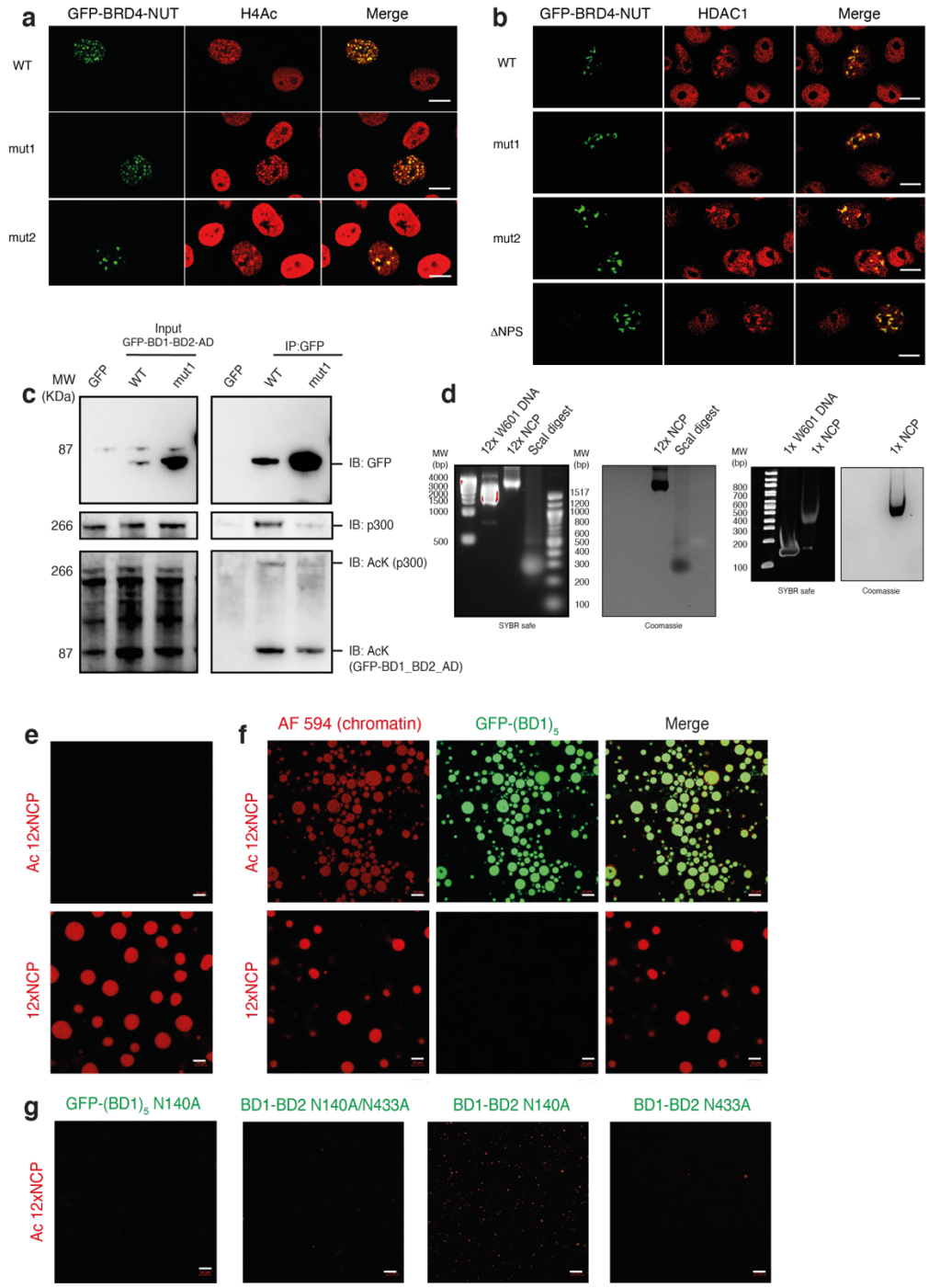


**Figure S5. Mechanism of condensation of BRD4-NUT and p300**. **a,** Colocalization of BRD4-NUT condensates with acetylated H4 (H4Ac) or **b**, with HDAC1. Cos7 cells were transfected with the indicated GFP-BRD4-NUT constructs and analysed by immunofluorescence using anti-H4Ac antibody and anti-HDAC1 antibody. Scale bars, 10 µm. **c**, Cos7 cells were co-transfected with HA-p300 and the indicated GFP-BRD4-NUT variants or GFP alone as the control. Co-immunoprecipitation (IP) experiments were performed using anti-GFP antibody and immuno-blotted (IB) for GFP, p300 and Acetylated-Lysine. (Left panel) Input samples were loaded as a control. Experiments were independently repeated at least three times. **d**, EMSA analysis of 12x nucleosome templates assembly (left) on 2% agarose (12xNCP) native gels. The 12x nucleosome template was digested with *ScaI* restriction enzyme to isolate single NCPs. (Right) EMSA analysis of mononucleosome (1x NCP) assembly on 5% native PAGE stained with Sybr safe or Coomassie Blue. **e**, Fluorescence microscopy images of AF594-labeled dodecameric nucleosome arrays. Non-acetylated 12x NCP chromatin formed droplets (bottom panel) that are dissolved after p300 acetylation (top panel). Scale bars, 10 µm. **f**, Acetylated and non-acetylated 12x NCP chromatin templates incubated with GFP-labelled BRD4 $(BD1)_5$. Scale bars, 10 µm. **g**, Acetylated 12x NCP chromatin templates incubated with GFP-labelled BRD4 $(BD1)_5$ N140A, BD1-BD2 N140A/N433A, BD1-BD2 N140A or BD1-BD2 N433A.

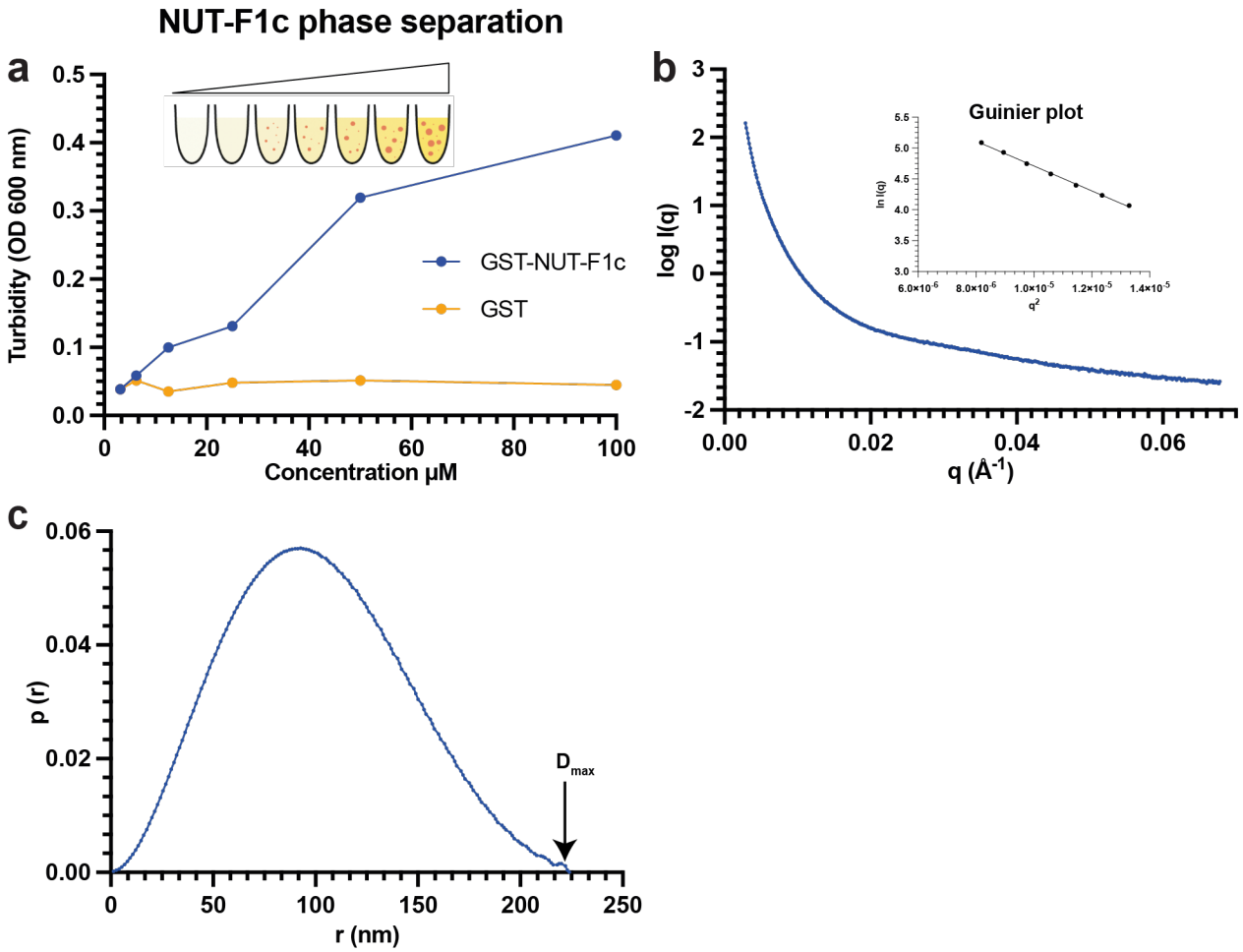


**Figure S6. Condensation is driven by bromodomain mulivalency**.
**a,** Concentration-dependent droplet formation of GST-NUT-F1c in droplet formation buffer with 125 mM NaCl and 10% PEG-8000 measured by turbidity. **b**, Experimental SAXS profile (log intensities calculated as a function of momentum transfer) for a 100 µM solution of GST-NUT-F1c in droplet formation buffer (blue). The Guinier region is inset. **c**, Distance distribution function.

**Movie S1. Dynamics of condensation of BD1-BD2-AD and p300.**
Time laps imaging. Left panel: GFP- BD1-BD2-AD. Middle: RFP-p300. Right: Merge of GFP- BD1-BD2-AD and RFP-p300.

**Movie S2. Dynamics of condensation of BRD4-NUT and p300.**
Time laps imaging. Left panel: GFP-BRD4-NUT. Middle: RFP-p300. Right: Merge of GFP-BRD4-NUT and RFP-p300.

**Table S1 – List of NUT constructs and binding experiments**

| Sample | Amino acid residues | Binding* |
|---|---|---|
| **NUT F1c** | 347-588 | + |
| **NUT1** | 347-446 | +/– |
| **NUT2** | 427-527 | + |
| **NUT3** | 508-588 | – |
| **NUT4** | 347-480 | + |
| **NUT5** | 347-514 | + |
| **NUT6** | 351-470 | + |
| **NUT7** | 448-492 | + |
| **NUT7 mut1** | 448-492 | + |
| **NUT8** | 396-470 | + |
| **NUT8 mut1** | 396-470 | – |
| **NUT8 mut2** | 396-470 | – |
| **NUT8 mut3** | 396-470 | + |
| **NUT8 mut4** | 396-470 | + |
| **NUT9** | 395-482 | + |
| **NUT10** | 468-482 | + |

*GST-pulldown, co-sedimentation or BLI

```
NUT7 wt:   PLALIEELEQEEGLTLAQLVQKRLMALEEEEDAEAPPSFSGAQLD
NUT7 mut1: PLALIEELEQEAGLTLAQAVQKRLMAAEEEEDAEAPPSFSGAQLD
NUT8 wt:   GQQQEEEGMYPDPGLLSYINELCSQKVFVSKVEAVIHPQFLADLLSPEKQRDPLALIEELEQEEGLTLAQLVQKRLMALEEEEDAE
NUT8 Mut1: GQQQEEEGMYPDPGAASAINEAASQKVAASKAEAAAHPQAAADAASPEKQRAPAGAIAAAAQAAGAALAQLVQKRLMALEEEEDAE
NUT8 Mut2: GQQQEEEGMYPKPGALSKINELGSQKVAGSKVSAGIHGQSLADGSSPEKQRKPLGSIEKSEQKSGGSLAQLVQKRLMALEEEEDAE
NUT8 Mut3: GQQQEEEGMYPDPGLLSYINELCSQKVFVSKVEAVIHPQFLADLLSPEKQRAPAGAIAAAAQAAGAALAQLVQKRLMALEEEEDAE
NUT8 Mut4: GQQQEEEGMYPDPGLLSYINELCSQKVFVSKVEAVIHPQFAADAASPEKQRAPAGAIAAAAQAAGAALAQLVQKRLMALEEEEDAE
```

**Table S2 - HADDOCK docking statistics**

| | |
|---|---|
| **Distance constraints** | |
| Ambiguous interaction restraints (AIRs) | 14 |
| Active residues on NUT7 | 5 |
| Active residues on TAZ2 | 9 |
| Intermolecular NOEs | 2 |
| **Dihedral angle restraints*** | |
| Phi/Psi | 5/5 |
| **Structural statistics** | |
| AIR Violations (mean ± s.d.) | 2±1 |
| Ramachandran analysis | |
| Residues in the favoured region (%) | 87% |
| Residues in the additional allowed regions (%) | 10% |
| Outliers | 3% |
| **Intermolecular energies after water refinement** | |
| $E_{vdw}$ (kcal mol$^{-1}$) | -45 ± 7 |
| $E_{elec}$ (kcal mol$^{-1}$) | -303 ± 32 |
| Buried surface area (Å$^2$) | 1498 ± 88 |

*Dihedral angle restraints derived from chemical shift values using TALOS-N are applied to NUT7 only. For the TAZ2 domain, the structure in PDB 2mzd is used as input to HADDOCK.

**Table S3 - Cryo-EM data collection and map reconstruction**

| | Nucleosome Core Particle |
|---|---|
| **Data collection** | FEI Titan Krios G3 |
| Detector | Gatan K3 direct electron detector |
| Voltage | 300 kV |
| Pixel size (Å) | 1.086 |
| Nominal Magnification | 81,000 |
| Dose rate on Detector ($e^{-}$ $sec^{-1}$ $px^{-1}$) | 15 |
| Dose rate on specimen ($e^{-}$ $sec^{-1}$ $px^{-1}$) | 17 |
| Defocus range (μm) | -2.3 to -1.1 |
| **Reconstruction** | |
| Symmetry imposed | C1 |
| Initial particle images (no.) | 80,764 |
| Final particle images (no.) | 33,202 |
| Resolution, FSC=0.143 (Å) | 6.61 |

**Table S4 – Quantification of condensation of BRD4-NUT variants***

| GFP-BRD4-NUT | RFP-p300 positive | RFP-p300 negative |
|---|---|---|
| **WT** | 100/100 | 100/100 |
| **mut1** | 99/100 | 89/100 |
| **mut2** | 100/100 | 92/100 |
| **BD1-BD2** | 16/100 | 0/100 |
| **BD1** | 18/100 | 0/100 |
| **BD2** | 99/100 | 99/100 |
| **K/E** | 21/100 | 3/100 |
| **ΔNPS** | 100/100 | 100/100 |
| **ΔBID** | 100/100 | 9/100 |
| **BD1-BD2-AD** | 99/100 | 1/100 |
| **BD1-BD2-ADmut1** | 0/100 | 0/100 |
| **BD1-BD2-E1A** | 94/100 | 91/100 |

* Foci forming cells/Total cell count

**Table S5 – Quantification of co-localization of BRD4-NUT and p300***

| GFP-BRD4-NUT | Pearson's R value | Co-localization ratio |
|---|---|---|
| **WT** | 0.81±0.01 | 0.90±0.02 |
| **ADmut1** | 0.84±0.01 | 0.87±0.02 |
| **ADmut2** | 0.76±0.02 | 0.90±0.01 |
| **ΔNPS** | 0.76±0.02 | 0.86±0.03 |

* At least 10 cells were analysed (n=10)

**Table S6 – Impact of Drug treatment on condensation**

| GFP-BRD4-NUT | JQ1 | A485 | TSA | CBP30 | 1,6-Hexandiol |
|---|---|---|---|---|---|
| **WT** | No | No | No | Yes | No |
| **ADmut1** | No | No | No | No | No |
| **ADmut2** | No | No | No | No | No |
| **ΔNPS** | No | No | No | Yes | No |

**Table S7 – Quantification of foci formation of after CBP30 treatment***

| GFP-BRD4-NUT | DMSO | CBP30 |
|---|---|---|
| **WT** | 100/100 | 54/100 |
| **ADmut1** | 92/100 | 3/100 |
| **ADmut2** | 91/100 | 2/100 |
| **ΔNPS** | 100/100 | 58/100 |

*Foci-forming cells/Total cell counted